POLITECNICO DI TORINO

Master Degree course in Mechanical Engineering

Master Degree Thesis

Multiscale mechanical modeling of lithium-ion battery module

Relatore

Prof. Aurelio Somà

Correlatore

Dott. Davide Clerici

Candidato

Salvatore Scalzo

Academic Year 2023-2024

I would like to dedicate this thesis to my loving parents and grandparents

Acknowledgements

I would like to express my deepest gratitude to my advisors, Prof. Aurelio Somà and Dott. Davide Clerici, for their invaluable guidance, support, feedback and patience throughout the course of my thesis. I am truly grateful for the time and effort they dedicated to helping me navigate challenges and refine my ideas.

I would like to extend my heartfelt thanks to my friends and colleagues who have been a constant source of support and encouragement throughout this journey.

Moreover, I would like to thank my dearest parents for their unconditional support, encouragement, and love throughout my academic journey. Your constant belief in me has been a powerful source of strength, and I am deeply grateful for the sacrifices you've made to help me pursue my dreams.

Abstract

Understanding multi-physics phenomena is crucial for accurately modeling and predicting the behavior of complex systems in engineering. Sometimes, accounting for the coupling across the various scales of the system is also important. In this work, these needs have driven extensive exploration into multi-physics and multiscale modeling with the software COMSOL Multiphysics, especially focusing on the homogenization technique. It is a method used to predict macroscopic properties of heterogeneous materials by analyzing a representative volume element (RVE) that reflects microscale variations. A multiscale approach in a multi-physics domain is then applied to lithium-ion battery pack. Nowadays, lithium-ion batteries (LIBs) are the most widespread energy storage system, covering a large field of applications. In the automotive and working vehicle industry, lithium-ion batteries are a strategic component affecting the design, the cost and the performance of the vehicle. The electrochemical processes which allow the battery to deliver or store electrical energy involve the interaction of lithium ions with the electrode microstructure causing its mechanical deformation, proportional to the concentration of lithium ions in the host material. The electrode microstructure strain results in mechanical degradation, reducing the overall battery's performance, and causes the macroscopic battery deformation. In this thesis, the macroscopic battery deformation originating from the electrode particles strain is analysed with a two-step homogenization process considering the coupling between mechanical, chemical and electrical behaviour. First, the composite electrode (made of active material particles, voids and conductive agents) is modelled with a representative volume element. Secondly, the battery is modelled homogenizing the contribution of the hundreds of composite electrode layers. The output of the model is then validated with experimental measurements quantifying the macroscopic battery deformation during operation. The second contribution of this work focuses on the impact of individual battery deformation on the entire battery pack. Furthermore, the constraint given by the battery pack

causes the change of the electrical performance of the battery itself, because of the compression of the microstructure of the electrodes. Then, different design solutions of the battery pack are investigated to optimize the battery performance and lifespan, while keeping a safe battery pack deformation.

Contents

List of Figures

List of Tables

Nomenclature

Roman Symbols

A	Electrodes surface $[m^2]$
a_s	Particles active surface area per unit volume $[m^2/m^3]$
$brugg$	Bruggeman coefficient [-]
c	Concentration $[mol/m^3]$
D	Diffusivity $[m^2/s]$
E	Young's modulus
F	Faraday constant $[C/mol]$
I	Current $[A]$
i	Current density $[A/m^2]$
J_{Li}	Lithium ion Flux $[mol/m^2 s]$
n	Moles $[mol]$
r	Radius $[m]$
R_c	Contact resistance $[\Omega m^2]$
R_g	Universal gas constant $[J/mol\,K]$
T	Temperature $[K]$
t	Thickness $[m]$
t_+	Transference number [-]
u	Displacement $[m]$
V	Volume $[m^3]$
x	Anode state of lithiation [-]
y	Cathode state of lithiation [-]

Acronyms

BCC	Body-Centered Cube
DFN	Doyle-Fuller-Newman
LIB	Lithium-ion Battery
OCP	Open Circuit Potential
P2D	Pseudo-Two-Dimensional
PDE	Partial Differential Equation
RVE	Representative Volume Element

Greek Letters

α_a	Anodic charge transfer coefficient [-]
α_c	Cathodic charge transfer coefficient [-]
ε	Porosity [-]

η	Overpotential $[V]$	l	Liquid-phase
κ	Electical conductiviy $[S/m]$	max	Maximum
ν	Poisson's ratio	r	Radial
Ω	Partial molar volume $[m^3/mol]$	s	Solid-phase
Φ	Potential $[V]$	$surf$	On particle surface
σ	Stress	**Superscripts**	
τ	Tortuosity [-]	an	Anode
ε	Strain [-]	cat	Cathode
ζ	Active material fraction [-]	ch	Chemical
Subscripts		e	Electrode
0	Initial	H	Homogenized
c	Circumferential	mec	Mechanical
h	Hydrostatic	p	Particle

Introduction

The aim of this thesis is the development of a multi-scale model to introduce battery modules in structural analysis accounting both for the internal electrochemical process and the external mechanical constraints during their operating conditions. The objective is to perform a detailed analysis without the need of modelling the whole internal structure of the module in the macroscale level. It can be done following the chemically induced deformations through scales and treating the battery as an homogeneous material despite its inhomogeneous structure in the lower scales. Therefore, the model is based on multi-scale approach and homogenization.

In the first chapter an introduction to lithium-ion batteries (LIBs) is presented: it is described their working principle, their main constituents and the corresponding used materials and their types of structure. A paragraph has been dedicated to safety issues that may occur.

In the second chapter the focus is on numerical simulations. Physical phenomena are usually described by sets of partial differential equations (PDEs) that can't be always solved easily in an analytical way. Due to the complexity of the analyzed geometry, non constant properties or multi-scale and multiphysics coupling, engineering problems need numerical ways to perform the sets of PDEs. The main focus is on finite element method (FEM) and examples of its applications.

In the third chapter are presented the types of LIBs modelling mainly focusing on the physics-based models. It is presented the Doyle-Fuller-Newman (DFN) electrochemical model and the contribution given by the mechanical coupling.

In the forth chapter the development of the homogenization-based multi-scale model is shown.

In the fifth chapter the developed model is applied to an LFP battery to be validated through experimental measurements previously performed. Additionally, after

the battery homogenization, the structural analysis of a battery module consisting of 18 LFP batteries is studied.

In the sixth chapter a conclusive summary of the model and its result is conducted.

Chapter 1

State of the art

1.1 Introduction

The ecological transition marks a pivotal moment in our relationship with energy, resources, and the environment. As the world grapples with the escalating impacts of climate change, the need to shift from conventional, polluting energy sources to more sustainable alternatives has never been more urgent. This transition is not just about reducing carbon emissions; it is about fundamentally rethinking how we produce, store, and use energy in a way that harmonizes with the planet's natural systems. Achieving this balance requires innovation that goes beyond merely generating energy. It requires advanced materials and systems capable of supporting a new era of sustainable energy use, systems that can store energy effectively, enable greater adoption of renewables, and reduce the overall environmental footprint of energy consumption. This transformation is at the heart of the ecological transition, a shift toward a future where humanity's energy needs are met without compromising the health of the planet or future generations.

Lithium-ion batteries (LIBs) have revolutionized modern technology, powering everything from smartphones and laptops to electric vehicles and renewable energy systems. They are the preferred energy storage solution due to their high energy density, duration, and relatively lightweight design [1]. The development of lithium-ion batteries began in the 1970s when scientists sought to create a rechargeable battery with higher energy density than existing technologies. The first commercially viable lithium-ion battery was introduced by Sony in 1991, marking a significant milestone

in energy storage. Since then, advancements in materials and manufacturing processes have continually improved their performance, safety, and cost-effectiveness [2].

One of the main contributions of battery technology is seen in the transportation sector, where electric vehicles (EVs) replace traditional internal combustion engines, significantly cutting greenhouse gas emissions and reducing the reliance on fossil fuels [3, 4]. The availability of materials like lithium, cobalt, and nickel is crucial for the sustainability and growth of lithium-ion batteries and for the impact on decarbonization [5]. Optimizing battery design improves efficiency, extends lifespan, and reduces reliance on scarce materials, enhancing overall performance and sustainability.

In the recent years, the attention on the mechanical behaviour of LIBs during their operating conditions has increased. In fact, the electrochemical phenomena are strictly coupled with the mechanical ones and, moreover, during the battery's operating conditions, a swelling/shrinking is induced to the system. From a modelling point of view, different multi-physics models have been proposed to entirely describe the LIBs behaviour [6, 7, 8]. From an experimental perspective, various tests have been conducted to measure the battery volume change induced by the electrochemical process using different methods: laser sensors [6, 9], load cells [10, 11], optic fibers (both embedded and external) [12, 13, 14], strain gauges [15, 16], internal pressure sensors [17, 18] and piezoelectric sensors [19].

One of the engineering challenge of the last years is the investigation of the structural behaviour of the batteries during their operating conditions as a part of a larger system. It is an interesting task for the mechanical optimization of the battery pack keeping it in safe conditions; the challenge is given by the complex multi-scale structure of the battery which can be overcome through multi-scale numerical model based on homogenization approach [20, 21]. The purpose of this work is to investigate and develop an homogenization-based multi-scale model.

1.2 Working principle and structure

LIBs operate on the principle of the movement of lithium ions between two electrodes, typically a graphite anode and a metal oxide cathode, through an electrolyte.

When the battery discharges, lithium ions flow from the anode to the cathode, releasing energy. During charging, this process is reversed, allowing the battery to store energy as shown in Figure 1.1. This mechanism allows for high efficiency and low self-discharge rates, making lithium-ion batteries highly reliable.

The energy flux is possible thanks to RED-OX reactions making the electrons e^- flow between the electrodes through an electric circuit, introducing a semipermeable membrane that separate anode and cathode. The semi-permeability of the membrane allows the Li^+ ions flow through the separator thanks to the presence of an electrolyte.

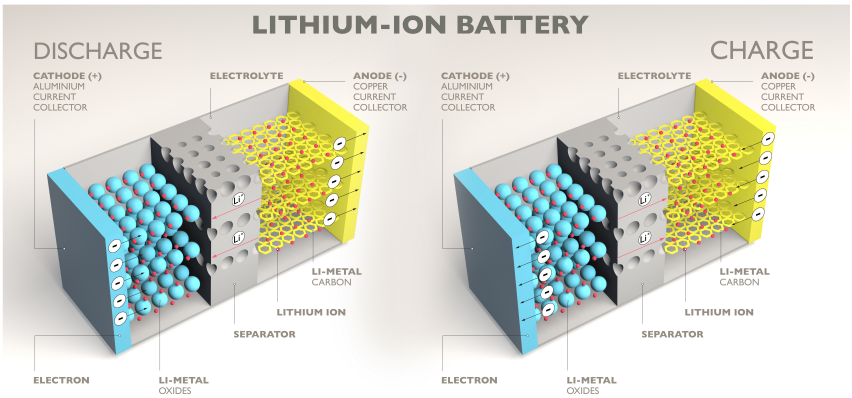

Fig. 1.1 Working principle of lithium-ion battery

1.2.1 Anode

The materials used for the anode are carefully chosen to optimize specific performance characteristics, such as the ability to store lithium ions, energy density, and the anode's longevity. The most common anode constitutive materials are:

- Graphite (C_6)
- Silicon (Si)
- Lithium Titanate (LTO)

The crystal structure of these lithiated (after the lithium ions insertion) materials is shown in Figure 1.2.

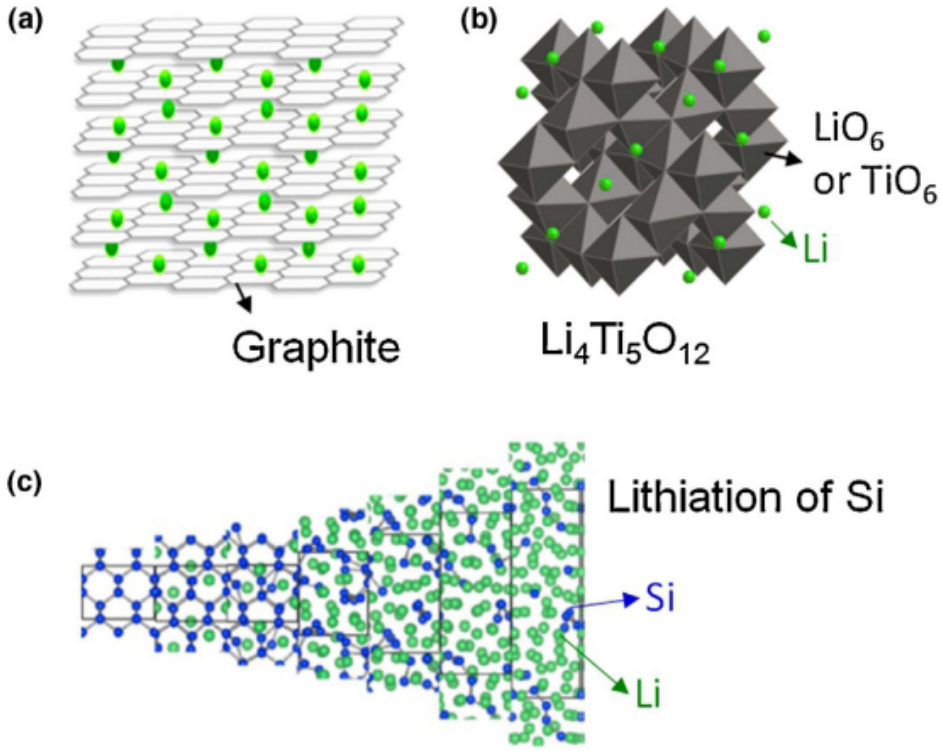

Fig. 1.2 Crystal structure of lithiated anode materials [22]

Graphite is the most widely used anode material in lithium-ion batteries due to its balance of performance, cost-effectiveness, and stability. It is a layered allotrope of carbon, where each layer consists of hexagonally arranged carbon atoms. These layers are held together by weak van der Waals forces, allowing lithium ions to easily intercalate between them during charging and deintercalate during discharging. The key characteristics that make graphite ideal as a negative electrode material in LIBs include:

- Intercalation Ability: Graphite allows lithium ions to insert and remove themselves reversibly between its layers, enabling repeated charge and discharge cycles.
- Stable Structure: The layered structure is highly stable, allowing durability.
- Low Operating Potential: Graphite operates at a low potential (around 0.1-0.2 V vs. Li/Li^+ in its higher specific capacity range as shown in Figure 1.3), close to that of lithium metal, enabling high energy densities.

- Abundance and Low Cost: Graphite is widely available and relatively inexpensive compared to alternative anode materials like silicon or lithium titanate.

Despite its advantages, graphite anodes have several limitations:

- The specific capacity of graphite (330-430 mAh/g) is much lower than silicon one (4200 mAh/g) [22]. This limits the overall energy density of lithium-ion batteries using graphite anodes, particularly for high-performance applications like electric vehicles.
- During fast charging or at low temperatures, lithium ions may not intercalate into the graphite layers efficiently. Instead, they can plate onto the surface of the anode as metallic lithium, which can lead to dendrite formation. Dendrites can pierce the separator, causing internal short circuits and potentially leading to battery failure or even fire hazards.
- A Solid Electrolyte Interphase (SEI) forms on the surface of the graphite anode during the first few charge cycles. This SEI layer is crucial for stabilizing the anode-electrolyte interface and preventing further reactions with the electrolyte, but it consumes lithium ions in the process, reducing the battery's initial capacity. Over time, the SEI can degrade or grow thicker, which can lead to increased impedance and reduced battery performance.
- Graphite anodes perform well under moderate charge/discharge rates, but under high-rate conditions their performance can degrade. This is due to the limited diffusion rate of lithium ions within the graphite structure, leading to lower power output and efficiency.

There are two primary types of graphite used in LIBs anodes: natural and synthetic. The former is mined from natural sources and processed into a fine powder suitable for battery applications, the latter is produced through high-temperature treatment of carbon precursors (such as petroleum coke). The synthetic graphite present higher production costs, purity and stability due to the manufacturing process.

On the other side, silicon has a much higher theoretical capacity than graphite, being able to store more lithium ions and to form silicon-lithium alloys ($Li_{15}Si_4$) during charging. However, silicon expands up to 300-400% when it alloys with

lithium during charging, leading to structural degradation, cracking, and loss of capacity over time [22, 23]. Lithium titanate is another alternative material for anodes, where lithium is stored in the titanium oxide spinel structure. It present improved safety characteristics compared to graphite because of higher operating voltage, reducing the risk of lithium plating, but it present lower energy density.

Researchers are experimenting with advanced carbon-based materials, including carbon nanotubes (CNTs), graphene, amorphous carbon and graphite-silicon. These materials have promising characteristics for high conductivity, fast charging, and high energy density [23].

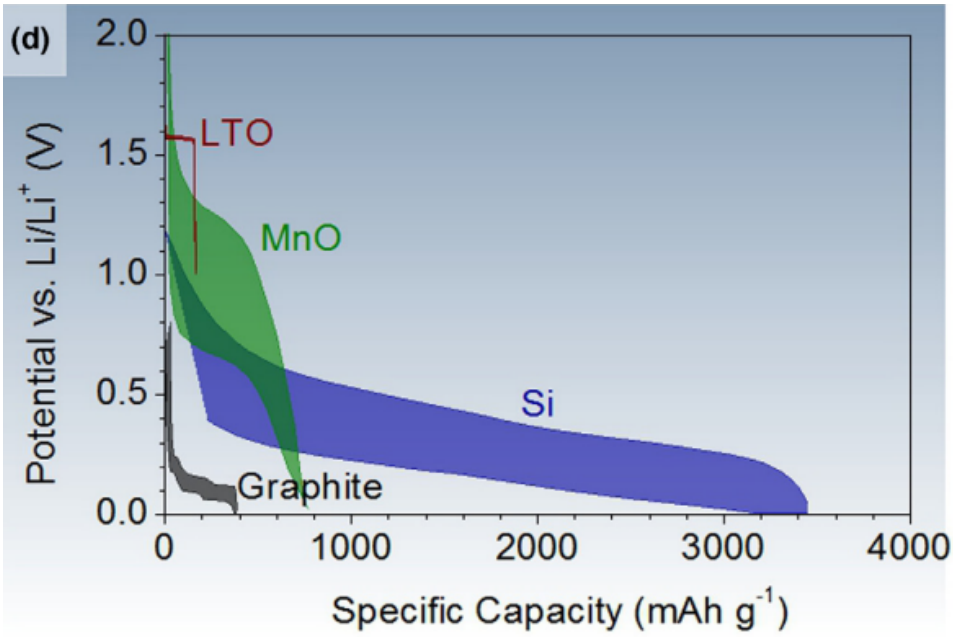

Fig. 1.3 Potential vs Specific Capacity of anode materials [22]

1.2.2 Cathode

As positive electrode, the cathode stores lithium ions during discharge and releases them during charging. Various materials are used as cathodes, each with distinct properties that impact the battery's energy density, cycle life, thermal stability, and cost. The performance and properties of LIBs are highly dependent on the cathode and different materials provide various trade-offs between the desired battery's properties. The most common types of cathode materials used in LIBs are described in the following list [22].

- Lithium Cobalt Oxide ($LiCoO_2$) - LCO

  LCO has a layered structure, with cobalt acting as the active material that facilitates the movement of lithium ions. It provides one of the highest energy densities among common cathode materials, making it ideal for small electronics like smartphones and laptops. LCO suffers from relatively low cycle life, especially under high charge and discharge rates. Cobalt-based cathodes can pose thermal runaway risks, making them more prone to overheating and combustion. Cobalt is expensive and has supply chain issues due to ethical and environmental concerns associated with mining.

- Lithium Nickel Manganese Cobalt Oxide ($LiNiMnCoO_2$) - NMC

  NMC is a layered material, with nickel, manganese, and cobalt acting in synergy to balance the performance. NMC cathodes offer a good balance between energy density, power, and lifespan. They are widely used in electric vehicles (EVs) due to their versatility. Additionally, it provides higher energy density than LFP ($LiFePO_4$) and LMO ($LiMn_2O_4$) while offering better safety than LCO. Higher nickel content improves energy density, but it can also reduce stability, requiring thermal management systems to ensure safety. Like LCO, NMC uses cobalt, which has cost and supply chain challenges.

- Lithium Iron Phosphate ($LiFePO_4$) - LFP

  LFP has an olivine structure, which is more stable than the layered structures of LCO and NMC. LFP is one of the safest cathode materials, with excellent thermal stability and resistance to thermal runaway. This makes it ideal for large-scale energy storage and electric buses. Iron and phosphate are abundant and inexpensive, making LFP a cost-effective option. LFP has a lower energy density than NMC and LCO, making it less ideal for applications where space and weight are critical, such as smartphones and EVs. The lower nominal voltage (3.2 V vs. 3.7 V for LCO) further reduces its energy density.

- Lithium Nickel Cobalt Aluminum Oxide ($LiNiCoAlO_2$) - NCA

  NCA is similar to NMC but uses aluminum as a stabilizing element instead of manganese. It offers some of the highest energy densities of any cathode material, making it suitable for high-performance applications like electric vehicles. NCA is less thermally stable than LFP, which means it requires more

sophisticated battery management systems to prevent overheating. Like the other cobalt-based cathode, it is characterized by high costs.

- Lithium Manganese Oxide ($LiMn_2O_4$) - LMO

  LMO has a spinel structure, which allows for fast lithium-ion diffusion and high power output, making it suitable for applications requiring fast charging and discharging, such as power tools and hybrid electric vehicles. Manganese is inexpensive, and LMO is relatively safe and thermally stable compared to LCO. However, LMO has a lower energy density than LCO, NMC, and NCA, limiting its use in energy-dense applications like long-range EVs. Additionally, tends to have a shorter cycle life due to capacity fading over time.

  The lattice structure of some of the lithiated cathode materials is shown in Figure 1.4.

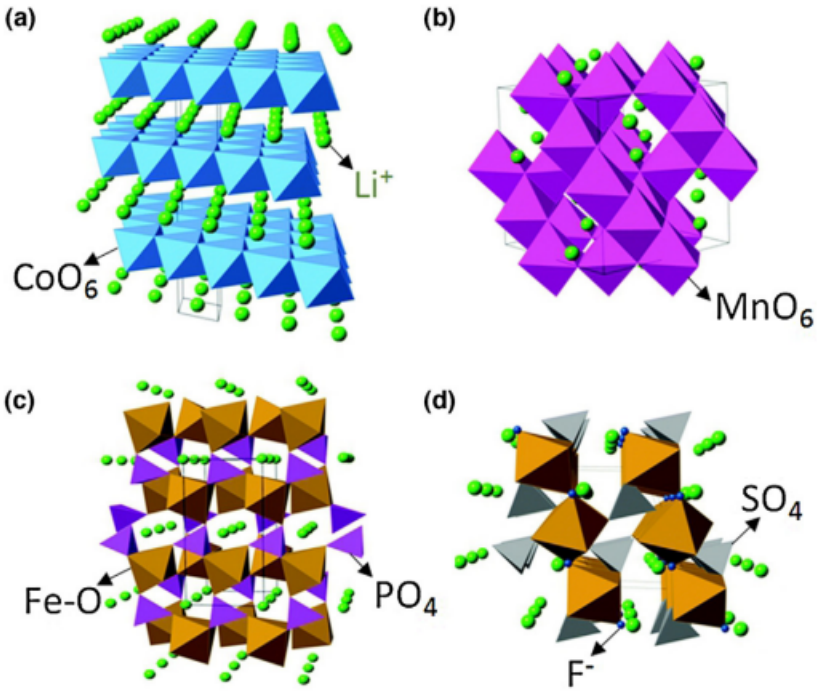

Fig. 1.4 Crystal structure of lithiated cathode materials [22]

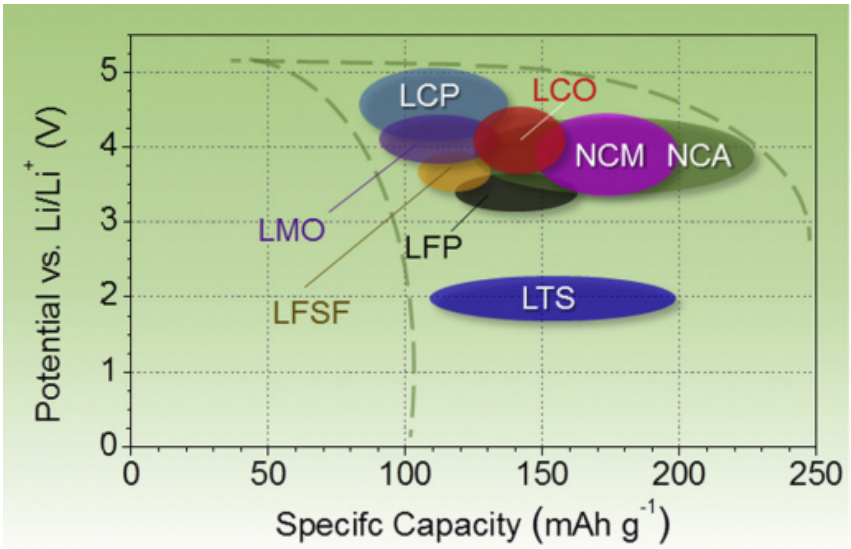

Fig. 1.5 Potential vs Specific Capacity of anode materials [22]

1.2.3 Electrolyte

The electrolyte's primary function in a lithium-ion battery is to transport lithium ions between the anode and the cathode through the process of ionic conduction, while preventing the movement of electrons between them. This separation of ions and electrons ensures that the electrochemical reactions at the electrodes occur correctly, facilitating charge storage and release. The electrolyte assists this ion transport without reacting with the electrodes or compromising the battery's safety and performance. There are three primary types of electrolytes used in LIBs: liquid electrolytes, solid electrolytes, and gel-based electrolytes. Each of these has distinct properties that affect the battery's performance, safety, and application range.

Liquid electrolytes are the most common type used in commercial lithium-ion batteries. They consist of a lithium salt dissolved in an organic solvent. Common salts include lithium hexafluorophosphate ($LiPF_6$), lithium bis(fluorosulfonyl)imide ($LiFSI$), and lithium tetrafluoroborate ($LiBF_4$). $LiPF_6$ is the most widely used due to its good balance between ionic conductivity and stability. The commonly used organic solvents are ethylene carbonate (EC), dimethyl carbonate (DMC), diethyl carbonate (DEC), and propylene carbonate (PC) whose structure is reported in Figure 1.6. They are characterized by low viscosity, high dielectric constants, and a wide electrochemical stability window [24].

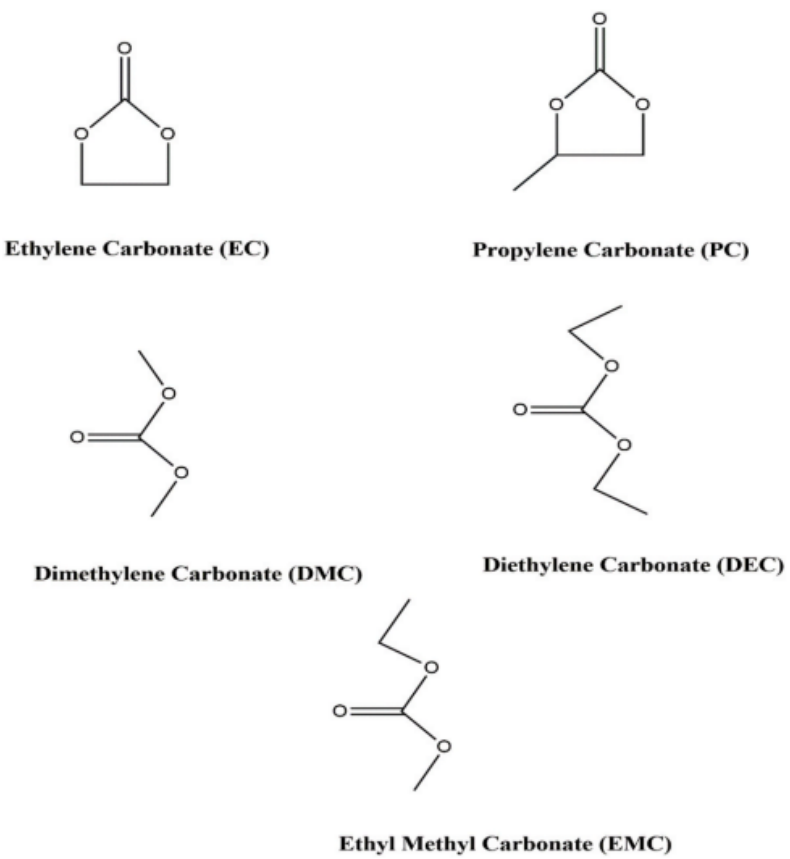

Fig. 1.6 Chemical structure of carbonate [24]

Solid-state electrolytes are a newer class of materials that can conduct lithium ions through a solid medium, offering several advantages over liquid electrolytes, especially in terms of safety and stability. In fact, organic solvents in liquid electrolytes are flammable, posing a risk of fire, particularly in high-temperature or overcharge conditions. Additionally, liquid electrolytes can degrade over time, especially at high voltages or in the presence of moisture, which can generate harmful byproducts like hydrofluoric acid (HF). However, solid electrolytes offer lower ionic conductivity, they should face challenges with the electrode-electrolyte interface and the manufacturing processes are currently more expensive than the liquid electrolyte ones [24].

Gel electrolytes are a hybrid solution between liquid and solid electrolytes. They consist of a liquid electrolyte immobilized within a polymer matrix, offering a

compromise between the high ionic conductivity of liquid electrolytes and the safety of solid-state ones [24].

1.2.4 Separator

The separator in a lithium-ion battery is a key component that physically divides the electrodes while allowing lithium ions to flow between them through the electrolyte. The separator is typically a thin, porous membrane made from materials like polyethylene (PE) or polypropylene (PP), designed to prevent direct contact between the electrodes - which would cause short circuit - while permitting ionic conductivity. A high-performance separator is crucial for battery safety, durability, and performance.

The separator must have sufficient porosity to allow the liquid electrolyte to fill the pores and enable free movement of lithium ions between the electrodes. Typical porosity ranges from 30% to 60%. The separator should also be thin enough to minimize resistance to ionic transport while maintaining mechanical strength. Additionally, it must be chemically inert and stable in contact with the electrolyte and electrodes and must withstand high temperatures without degrading.

The most common materials used for separators in LIBs are polyolefins (polyethylene and polypropylene), which are chosen for their cost-effectiveness, mechanical properties, and ability to shut down the battery at high temperatures through a thermal shutdown mechanism: when the temperature rises above a certain point (e.g., around 130°C for PP and 150°C for PE), the separator will melt, closing its pores and blocking ionic movement. This interrupts the battery's operation, preventing further heat generation and lowering the risk of thermal runaway. To improve the thermal stability of polyolefin separators, some separators are coated with a thin layer of ceramic materials like aluminum oxide (Al_2O_3) or silicon dioxide (SiO_2) [25].

Evolving toward solid-state batteries, which replace liquid electrolytes with solid electrolytes, separators may play a reduced role. However, in the transition to solid-state batteries, hybrid separators that are compatible with both solid and liquid electrolytes are being explored.

1.2.5 Current Collectors

Current collectors facilitate the flow of electrons between the external circuit and the active materials of the anode and cathode. They do not participate in the electrochemical reaction but play a crucial role in conducting electricity. The main current collectors used in LIBs are typically metal foils, with copper (Cu) used for the anode and aluminum (Al) for the cathode.

Copper is used because of its excellent electrical conductivity and resistance to corrosion. It can handle the lower potentials of the anode without reacting or degrading. Aluminum is chosen for the cathode because of its low density, good conductivity, and electrochemical stability at the higher potentials found at the cathode. It cannot be used for the anode due to its tendency to alloy with lithium at low potentials, which would degrade its performance.

1.2.6 Configurations

Three main types of geometrical configurations of lithium-ion batteries can be distinguished and their naming reflects their shapes and packaging style: cylindrical, prismatic and pouch as shown in Figure 1.7.

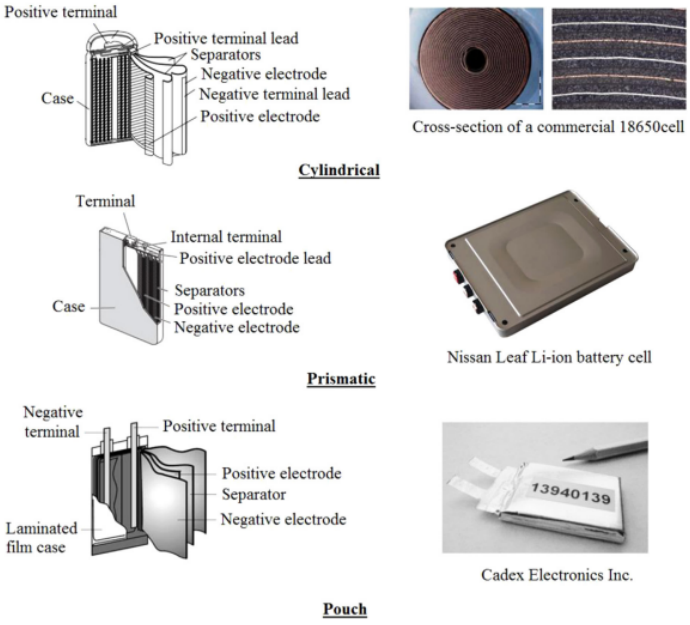

Fig. 1.7 Lithium-ion batteries configurations [26]

Cylindrical cells are among the oldest and most widely used battery formats. They are commonly used in laptops, power tools, electric vehicles and other portable electronics. The cylindrical shape provides excellent structural integrity and is resistant to swelling and damage. Their round design allows for good heat dissipation, which is important for maintaining battery health and preventing overheating. However, they present low space efficiency, leading to lower energy density due to their shape.

Prismatic cells have a rectangular, box-like design. They are typically encased in a hard metal housing, which gives them a solid structure but makes them slightly bulkier compared to other formats. Prismatic cells make better use of available space within devices because of their flat, rectangular shape, which allows them to be packed closely together. Their form factor allows for a higher energy density compared to cylindrical cells in a given volume. Prismatic cells are widely used in automotive applications (electric vehicles), consumer electronics, and large-scale energy storage systems (such as grid storage).

Pouch cells use a flexible, laminated, and sealed aluminum plastic film rather than a rigid metal casing. This flexible packaging allows for a slim, flat profile and greater adaptability to the shape of the device they are powering. They are commonly found in mobile phones, tablets, laptops, drones, and some electric vehicles (e.g., BMW i3). The lack of a rigid case allows pouch cell to achieve high energy density and a lighter design. On the other side, they are prone to swelling over time, especially when overcharged or under heavy use and they are vulnerable to physical damage.

1.3 Safety issues and degradation

Lithium-ion batteries, despite their widespread use and efficiency, present several safety challenges that must be carefully managed to prevent dangerous outcomes. The damage of lithium-ion battery is mainly connected induced by three sources: mechanical, electrical and thermal (Figure 1.8).

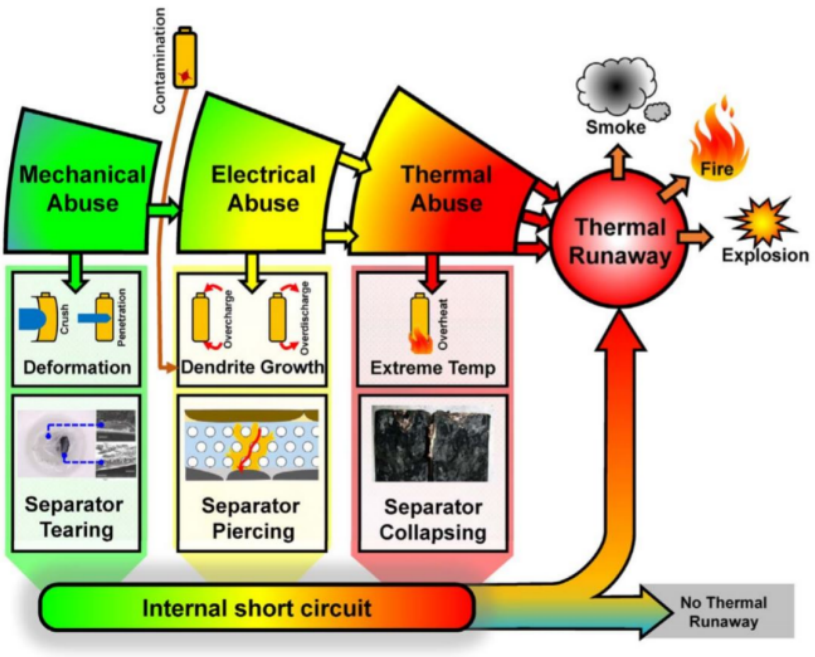

Fig. 1.8 Sources of LIBs damage [27]

Mechanical abuse, consisting in vibration or crush and penetration due to collisions, could induce damage in batteries which leads to capacity and power fade or more severe consequence as short circuit. In fact, collision can cause the internal structure collapse making positive and negative electrode in touch causing internal short circuit.

Electrical abuse mainly happens as a result of external short circuit and overcharging. An external short circuit happens when the battery's positive and negative terminals are directly connected by a conductive material outside the battery, creating a low-resistance path. When this happens, the battery discharges rapidly, generating a large current. The immediate effect is intense heat generation, which can damage the battery's internal components and potentially lead to thermal runaway, a situation where the heat produced triggers further reactions, escalating to a fire or explosion. To prevent such outcomes, many batteries include safety systems that detect the excessive current flow and disconnect the circuit before the situation worsens. Overcharging, on the other hand, happens when the battery is charged beyond its designed voltage limits. Lithium-ion batteries have a narrow voltage range in which they operate safely, typically with an upper limit of around 4.2V per cell. Exceeding this limit can cause the battery to degrade in several ways. One of the main problems

is lithium plating, where metallic lithium forms on the anode instead of properly intercalating into the material. This not only reduces the battery's efficiency and capacity but also poses a significant risk of internal short circuits due to dendrite formation. Additionally, overcharging can cause the electrolyte inside the battery to decompose, leading to gas formation, swelling, and increased internal pressure, which can lead to the battery venting or even bursting.

One of the most critical issues is thermal runaway, a situation where excessive heat accumulates within the battery, often due to the mechanical and electrical abuse mentioned before. This process can escalate rapidly, triggering a chain reaction that leads to cell rupture, fires, or even explosions. The most dangerous source of thermal abuse are the internal short circuits. Generally the danger of the internal short circuit can be divided in three levels as shown in Figure 1.9.

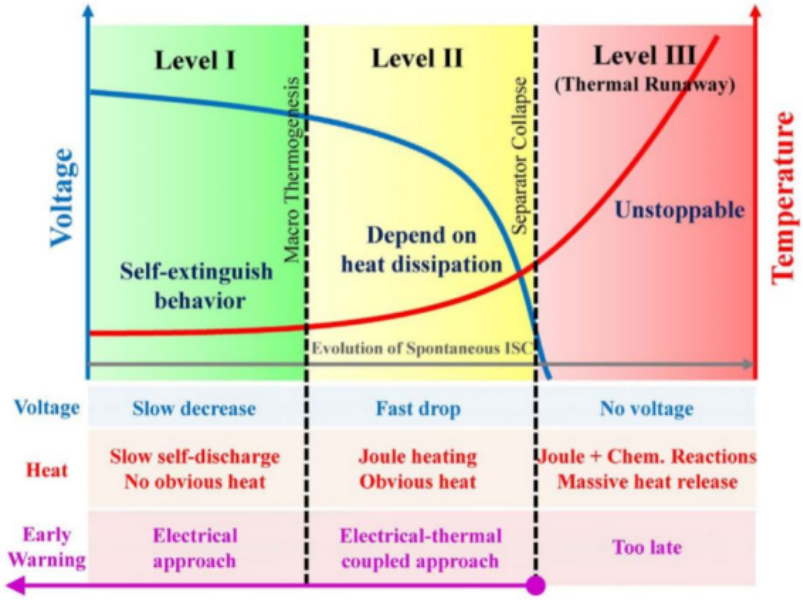

Fig. 1.9 Levels of internal short ciruit danger [27]

Mechanical and electrochemical problems, such as solid electrolyte interphase (SEI) layer degradation and lithium plating, also play a significant role in battery performance and safety.

The SEI layer, a thin film that forms on the anode during initial cycling, is crucial for battery stability. This layer acts as a protective barrier, preventing further reactions between the electrolyte and the anode. However, the SEI is not static: it

can degrade, crack, or reform during cycling, especially under extreme conditions like high charging rates or low temperatures. When the SEI layer breaks down, it exposes fresh anode material to the electrolyte, leading to unwanted reactions and electrolyte depletion. This can cause a loss of battery capacity, increased internal resistance, and, in some cases, gas formation inside the cell, leading to swelling and increased risk of thermal runaway.

Lithium plating is another serious issue, typically occurring when a battery is charged too quickly or at low temperatures. Under these conditions, lithium ions do not intercalate smoothly into the anode material (usually graphite), and instead, metallic lithium begins to deposit on the anode surface. This metallic lithium forms dendrites—needle-like structures that grow during repeated cycling. If these dendrites grow long enough, they can pierce through the separator between the anode and cathode, causing an internal short circuit. This not only reduces the battery's capacity and efficiency but can also lead to dangerous events such as overheating, fires, or explosions.

Chapter 2

Numerical Methods

Complex engineering and mathematical problems often involve geometries, material properties, or boundary conditions that make reaching exact solutions through traditional analytical methods difficult or impossible. For instance, problems involving stress analysis in irregularly shaped structures, fluid flow around objects or heat distribution in materials with varying properties cannot be solved with simple formulas. These problems are typically governed by partial differential equations (PDEs), which describe how physical quantities change over space and time.

Analytical solutions to PDEs are often limited to idealized conditions with simplified assumptions, like uniform materials or symmetrical shapes. However, real-world problems rarely conform to these ideal situations. This is where numerical methods, like the Finite Element Method (FEM), Finite Difference Method (FDM) or Finite Volume Method (FVM), become essential: they allow engineers and scientists to find approximate solutions for these complex problems solving PDEs in a different way.

2.1 Multiphysics

In physics and engineering, each physical phenomenon is governed by its own set of partial differential equations, for instance:

- Structural Mechanics is represented by the equations of elasticity which describe how solid materials deform under stress and, vice versa, how they are

stressed under deformations. This set of PDEs consists in three equilibrium equations and six compatibility equations linked by material constitutive laws.

- Heat Transfer is described by the heat equation, a PDE that explains how temperature evolves over time within a material. It accounts for conduction, convection and radiation, capturing how heat flows from high to low-temperature areas.

- Chemical Reactions are represented by the reaction-diffusion equations describing how chemical concentrations change over time and space. These PDEs are used to model processes like diffusion in a fluid, where chemicals spread out, and reaction kinetics, where substances transform into different products.

- Electromagnetics is governed by Maxwell's equations. They describe how electric and magnetic fields propagate and interact with materials. These are crucial for designing devices like antennas, sensors, and electrical circuits.

- Fluid Dynamics is governed by The Navier-Stokes equations that describe fluid flow, including velocity, pressure, and turbulence. These set of equations account for how fluids behave under different forces and conditions, such as airflow over an aircraft wing.

Each of these PDEs represents a single physical domain, but real-world problems often involve multiple interacting physical phenomena. For example, in a battery, there is need to understand heat generation (heat transfer), chemical reactions and electrical conduction (electrochemistry), mechanical deformation and damage (structural mechanics) simultaneously. This is known as multiphysics analysis.

Coupling different physics is often challenging because the equations are interdependent and may operate on different scales. Solving these coupled equations requires sophisticated numerical techniques and computational power, as traditional analytical methods usually can't handle the complexity of these interactions. This makes multiphysics simulation environments essential in fields like aerospace, electronics, and energy systems, where accurate modeling of coupled phenomena is crucial for design and optimization. Although, attention is needed during the discretization phase because the proper elements needed for a certain physical phenomena could be inconsistent or not enough for others.

2.2 Finite Element Method

The Finite Element Method (FEM) consists in finding a numerical solution in integral form on a finite domain from a physical-mathematical problem described by PDEs. The general approach consists in:

1. Finding an integral functional on a finite domain from the differential problem.
2. Discretizing the continuous domain introducing approximation functions.
3. Obtaining a matrix problem substituting the approximation functions in the functional expression.

Therefore, two crucial aspects of the finite element methode are:

- Describing the set of PDEs with the proper integral functional.
- Introducing the proper geometrical and mathematical discretization.
  - Geometrical to break down the infinite degrees of freedom continuous domain into a finite element domain.
  - Mathematical to describe the single element with the corresponding approximation function.

The discretization will introduce elements and nodes. The elements are the discrete parts of the problem's continuous domain and they interconnected at nodes that is where the matrix problem is solved. The other points inside the element will follow the nodes behaviour through the approximation functions that should interpolate the solution variable at the nodes of the element [28]. In this section, FEM approach is applied to structural mechanics, heat transfer and chemical reactions that are the main LIBs physical domains. Figure 2.1 describe a typical numerical simulation workflow.

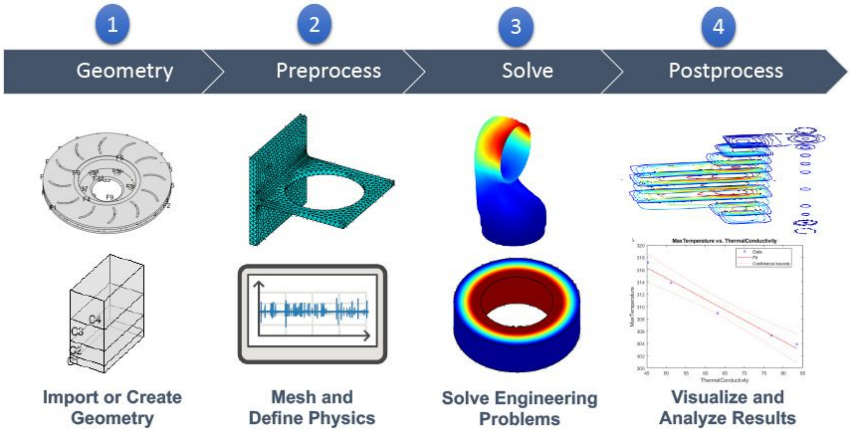

Fig. 2.1 Typical finite element method workflow

2.2.1 Structural Mechanics

The Finite Element Method is widely used in structural mechanics for analyzing and solving problems involving the behavior of structures under various loads and conditions. One of the FEM approach to structural mechanics is exploiting the virtual work principle as following presented.

Analyzing an infinitesimal cube of material -under a coherent generic stress state (as shown in Figure 2.2) - the equilibrium equation along the j-th direction is described by Equation 2.1.

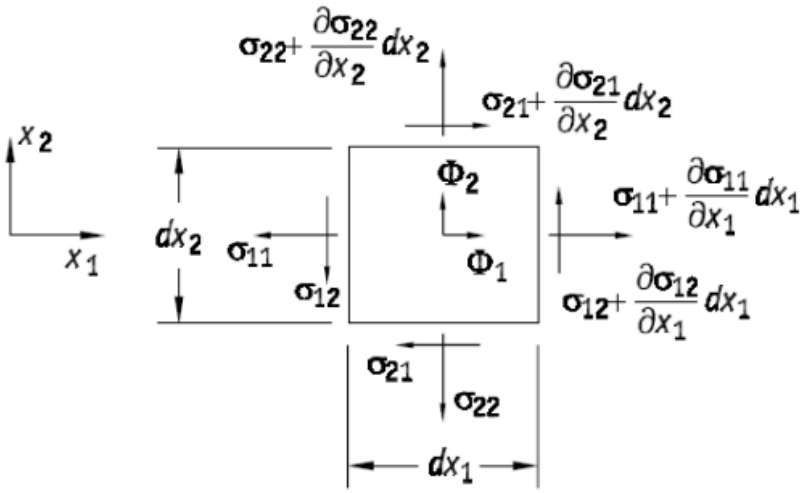

Fig. 2.2 Virtual work principle - Stress

$$\sum_{i=1}^{3} \frac{\partial \sigma_{ij}}{\partial x_i} + \phi_j = 0 \tag{2.1}$$

Assuming a coherent virtual displacement field (as shown in Figure 2.3), the virtual work of the infinitesimal cube is a scalar obtained multiplying the infinitesimal force ($dF = \sigma dA$) by the corresponding virtual displacement and summing all the contributions. The infinitesimal virtual work for the i-th (dW_i) direction is expressed by the Equation 2.2:

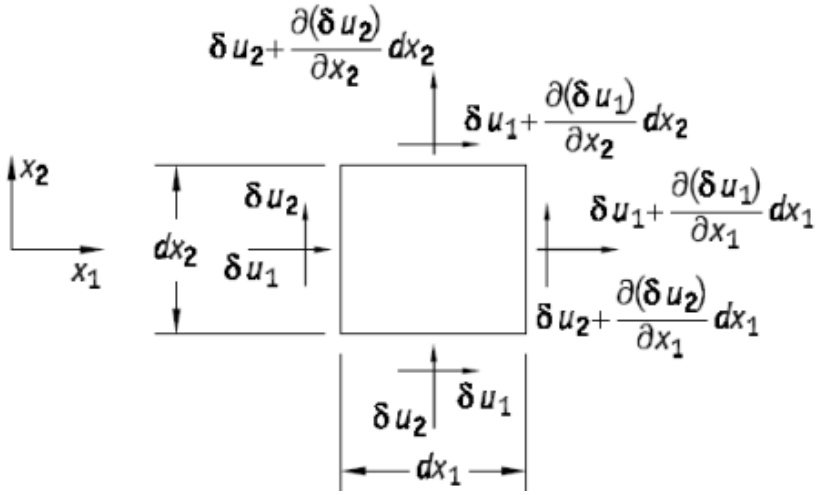

Fig. 2.3 Virtual work principle - Virtual displacement

$$dW_i = \sum_{k=1}^{3} [-\sigma_{ik}\delta u_k dA_i + (\sigma_{ik} + \frac{\partial \sigma_{ik}}{\partial x_i} dx_i)(\delta u_k + \frac{\partial (\delta u_k)}{\partial x_i} dx_i) dA_i] \tag{2.2}$$

Summing the contribution in the three directions and ignoring the higher order infinitesimal terms, the internal virtual work can be expressed as following:

$$dW_{int} = \sum_{i=1}^{3} \sum_{k=1}^{3} (\frac{\partial \sigma_{ik}}{\partial x_i} \delta u_k + \sigma_{ik} \frac{\partial (\delta u_k)}{\partial x_i}) dV \tag{2.3}$$

The virtual work equation can be rearranged using the equilibrium and compatibility equations inside the two terms.

- The i-th summation of the first term is the equilibrium equation along the k-th direction. Substituting the Equation 2.1 inside this term, the following scalar product is obtained:

$$\sum_{i=1}^{3}\sum_{k=1}^{3}\frac{\partial \sigma_{ik}}{\partial x_i}\delta u_k = -\sum_{k=1}^{3}\phi_k \delta u_k = -\{u\}^T\{\phi\} \tag{2.4}$$

- Due to linearity of the partial derivative and the small virtual displacement:

$$\frac{\partial}{\partial x_i}(\delta u_k) = \delta\frac{\partial u_k}{\partial x_i} \tag{2.5}$$

Compatibility equations can be applied in Equations 2.5, so that:

$$\frac{\partial u_i}{\partial x_i} = \varepsilon_i \quad , \quad \frac{\partial u_j}{\partial x_i} + \frac{\partial u_i}{\partial x_j} = \gamma_{ij} \tag{2.6}$$

Due to reciprocity of shear strain and summing all the above considerations, the second term of Equation 2.3 can be rearranged obtaining another scalar product:

$$\sum_{i=1}^{3}\sum_{k=1}^{3}\sigma_{ik}\frac{\partial(\delta u_k)}{\partial x_i} = \sum_{i=1}^{3}\sum_{k=1}^{3}\sigma_{ik}\delta\frac{\partial u_k}{\partial x_i} = \{\varepsilon\}^T\{\sigma\} \tag{2.7}$$

Therefore, substituting the Equations 2.4 and 2.7 inside the infinitesimal internal virtual work expression:

$$dW_{int} = (\{\varepsilon\}^T\{\sigma\} - \{u\}^T\{\phi\})dV \tag{2.8}$$

To obtain the entire internal virtual work, Equation 2.8 should be integrated in the corresponding domain.

$$W_{int} = \int_V \{\varepsilon\}^T\{\sigma\}dV - \int_V \{u\}^T\{\phi\}dV \tag{2.9}$$

The internal virtual work should be balanced by the external one coming from the external forces acting on the infinitesimal cube boundaries as shown in Figure 2.4.

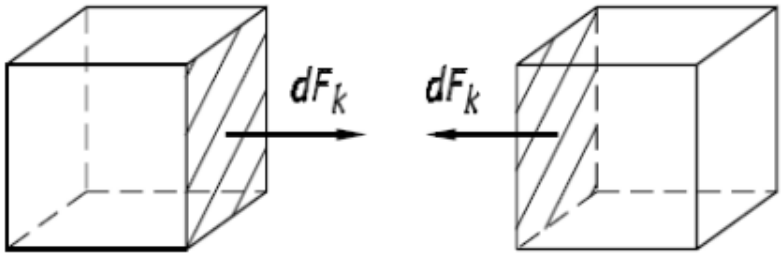

Fig. 2.4 Virtual work principle - External forces

$$W_{ext} = \sum_{k=1}^{3} \int_A t_k \delta u_k dA = \int_A \{\delta u\}^T \{t\} dA \tag{2.10}$$

Equaling the Equations 2.9 and 2.10, a unique equation, representing an energy balance, is obtained. This expression contains the three equilibrium and the six compatibility equations in a matrix problem.

$$\int_V \{\varepsilon\}^T \{\sigma\} dV - \int_V \{u\}^T \{\phi\} dV = \int_A \{\delta u\}^T \{t\} dA \tag{2.11}$$

The structural mechanics set of PDEs is completely represented by the integral functional obtained with the virtual work principle thanks to the stiffness matrix that links stress and strain. In structural mechanics, the solution variable is the displacement $\{u\}$. The approximation functions that link the solution variable inside the domain and the computed solution in the nodes $\{s\}$ are called shape functions $[n]$ (Equation 2.12).

$$\{u\} = [n]\{s\} \tag{2.12}$$

Due to compatibility equations, a partial derivative matrix $[\partial]$ can be introduced to compute the strain vector from displacement. Through the stiffness matrix, also the stress vector can be obtained from the strain one and consequently through displacement.

$$\{\varepsilon\} = [\partial]\{u\} = [\partial][n]\{s\} = [b]\{s\} \tag{2.13}$$

$$\{\sigma\} = [E]\{\varepsilon\} = [E][b]\{s\} \tag{2.14}$$

Due to the approximation of the solution variable inside the element domain, the equilibrium equation won't be satisfied at each point: a residual force should be introduced in Equation 2.1.

$$\sum_{i=1}^{3} \frac{\partial \sigma_{ij}}{\partial x_i} + \phi_j = \rho_j \tag{2.15}$$

Additionally, the surface load $\{t\}$ is split in known and unknown loads, $\{t_0\}$ and $\{t^*\}$ respectively. Accounting for these relationships, the matrix problem obtained from the virtual work principle is:

$$\begin{aligned} &\{\delta s\}^T \int_A [n]^T \{t^*\} dA - \{\delta s\}^T \int_V [n]^T \{\rho\} dV + \\ &+ \{\delta s\}^T \int_V [n]^T \{t_0\} dA + \{\delta s\}^T \int_V [n]^T \{\phi\} dV = \\ &= \{\delta s\}^T \int_V [b]^T [E][b] dV \{s\} \end{aligned} \tag{2.16}$$

The energy balance of the virtual work principle becomes an equilibrium equation because it doesn't depend on virtual displacement $\{\delta s\}$. Therefore, Equation 2.16 can be written as:

$$\{f\} + \{f_e\}_{t_0} + \{f_e\}_{\phi} = [k]\{s\} \tag{2.17}$$

- $\{f\} = \int_A [n]^T \{t^*\} dA - \int_V [n]^T \{\rho\} dV$ are the nodal loads,
- $\{f_e\}_{t_0} = \int_V [n]^T \{t_0\} dA$ are the surface loads,
- $\{f_e\}_{\phi} = \int_V [n]^T \{\phi\} dV$ are the body forces,
- $[k] = \int_V [b]^T [E][b] dV$ is the stiffness matrix.

Computing the virtual work equation in dynamic conditions, two additional terms are involved: a damping work and an inertial one, whose forces are proportional to velocity and acceleration respectively.

$$[m]\{\ddot{s}\} + [c]\{\dot{s}\} + [k]\{s\} = \{f\} + \{f_e\}_{t_0} + \{f_e\}_{\phi} \tag{2.18}$$

- $[m] = \int_V \rho [n]^T [n] dV$ is the mass matrix and ρ is the density,
- $[c] = \int_V c_s [n]^T [n] dV$ is the damping matrix and c_s is the damping coefficient.

The dynamic transient analysis can be performed through modal superposition or direct integration method.

2.2.2 Heat Transfer and Chemical Reactions

Heat transfer is the process of energy moving from one system to another due to a temperature difference. The heat equation is a mathematical representation of heat transfer, describing how temperature changes over time and space in a given material due to conduction. The heat equation, also called Fourier's equation, has the following form:

$$\rho c_p \frac{\partial T}{\partial t} - \nabla \cdot (\lambda \nabla T) = f \tag{2.19}$$

where ρ is the density, c_p is the specific heat, λ is the thermal conductivity and f is the forcing term.

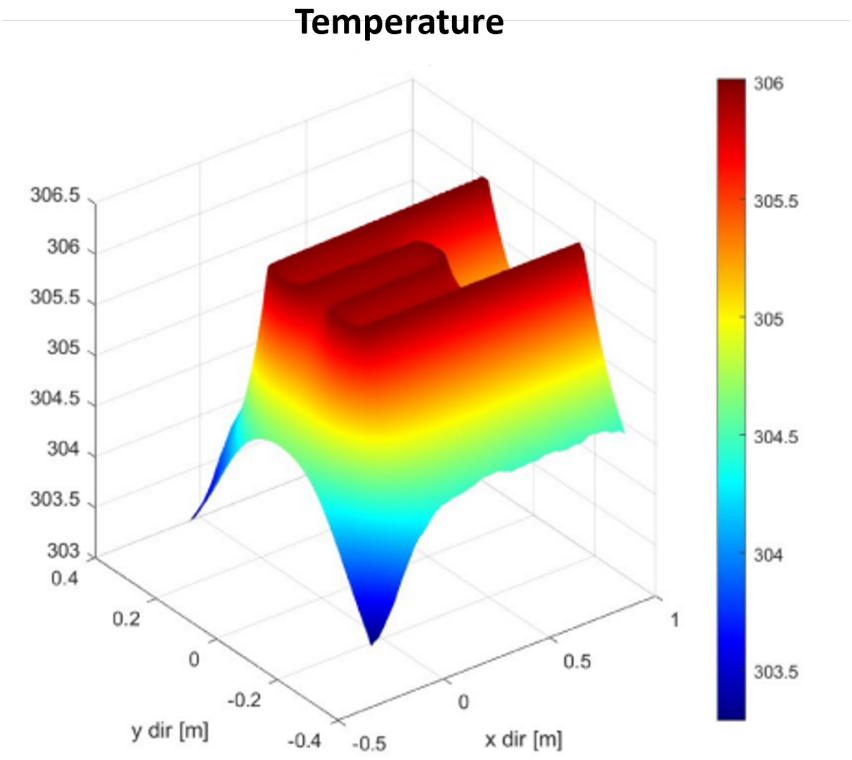

Fig. 2.5 Example of thermal analysis

A chemical reaction is a process where reactants are transformed into products through the breaking and forming of chemical bonds. Chemical reactions can be linked to Fick's laws, especially when diffusion plays a crucial role. These two equations describe how particles or molecules spread from regions of high concentration to low concentration over time. The combination of the first and the second Fick's laws leads to the following expression:

$$\frac{\partial c}{\partial t} - \nabla \cdot (D \nabla c) = \phi \tag{2.20}$$

where D is the diffusivity and ϕ is a source term.

Equations 2.19 and 2.20 have the same differential form [29]: a common procedure, with a generic solution variable u, can be found to obtain the same matrix problem; the proper coefficients will then be substituted in their corresponding equation. In this case, the matrix problem is obtained through a variational method that is explained below in a simple condition and then generalized.

A generic 1D phenomenon is described by the following differential problem:

$$\begin{cases} -\frac{d}{dx}(\mu \frac{du}{dx}) = f \quad in \quad (0,L) \\ u(x=0) = u(x=L) = 0 \end{cases} \tag{2.21}$$

The variational formulation of the differential problem is obtained through the following steps.

1. Multiply the differential formulation times a test function v that should belong to the vector space V:

$$v \in V : \{v \in C^0([0,L]), v \in C^1([x_i, x_{i+1}] \in [0,L]), v(0) = v(L) = 0\}$$

2. Integrate the obtained formulation in the problem domain:

$$\int_0^L -\frac{d}{dx}(\mu \frac{du}{dx}) \cdot v dx = \int_0^L f \cdot v dx \quad \forall v \in V \tag{2.22}$$

3. Rearrange the above expression integrating by part the left side.

$$\int_0^L \mu \frac{du}{dx} \cdot \frac{dv}{dx} dx = \int_0^L f \cdot v dx + (\mu \frac{du}{dx} \cdot v\big|_L - \mu \frac{du}{dx} \cdot v\big|_0) \quad \forall v \in V \tag{2.23}$$

The differential formulation expressed as Equation 2.21, which is generally a vector equation, is now expressed as a scalar integral equation which is the variational formulation. It is the same result reached in structural mechanics with virtual work principle moving from a force equilibrium to an energy balance.

Accounting for the Dirichlet boundary conditions, the continuous variational formulation is expressed as following:

$$\begin{cases} Find\ u \in V : \\ \int_0^L \mu \frac{du}{dx} \cdot \frac{dv}{dx} dx = \int_0^L f \cdot v dx \quad \forall v \in V \end{cases} \tag{2.24}$$

As already did in structural mechanics, meshing the domain and introducing elements, nodes and the approximation functions, the computation moves from the continuous formulation to the discrete one. It is sufficient that the Equation 2.24 is valid in a subspace V_h of V:

$$\begin{cases} Find\ u_h \in V_h : \\ \int_0^L \mu \frac{du_h}{dx} \cdot \frac{dv_h}{dx} dx = \int_0^L f \cdot v dx \quad \forall v_h \in V_h \subset V \end{cases} \tag{2.25}$$

Being a finite vector space, V_h has its own basis: each vector v_h can be written as a linear combination of the vector basis $\varphi_1, \ldots, \varphi_i, \ldots, \varphi_n$:

$$v_h = \sum_{i=1}^{n} v_i \varphi_i \tag{2.26}$$

Consequently, it is not necessary that the Equation 2.25 is valid for all v_h but it is sufficient that it is true for the element of the basis. For this reason and writing u_h as a linear combination of the basis vectors:

$$\sum_{i=1}^{n} (u_i \int_0^L \mu \frac{d\varphi_i}{dx} \frac{d\varphi_j}{dx} dx) = \int_0^L f \varphi_j dx \quad \forall j = 1, ..., n \tag{2.27}$$

Therefore, the j-th equation and the whole matrix problem can be expressed as shown in Equation 2.28.

$$[a_{j1} \cdots a_{ji} \cdots a_{jn}] \begin{bmatrix} u_1 \\ \vdots \\ u_i \\ \vdots \\ u_n \end{bmatrix} = f_j \quad \Longrightarrow \quad [A]\{u\} = \{f\} \tag{2.28}$$

This matrix form is analogous to Equation 2.17 and, consequently, the matrix $[A]$ is called "FEM stiffness matrix" whose generic element depends on the approximation functions as $[k]$. In this 1D case:

$$a_{ji} = \int_0^L \mu \frac{d\varphi_i}{dx} \frac{d\varphi_j}{dx} dx \tag{2.29}$$

but it can be extended to non-1D differential problems substituting the derivative of the basis vectors with their gradient because $\varphi_{1D}(x) \rightarrow \varphi_{3D}(x, y, z)$.

If the differential problem is time dependent, a "FEM mass matrix" $[B]$ should be introduced - as already done with the stifness one - moving from the differential

formulation to the variational one. This time, it is directly done with the Fick's law in a generic 3D domain Ω. The variational formulation of Equation 2.20 is expressed in Equation 2.30.

$$\begin{cases} Find\ c_h \in V_h : \\ \int_\Omega \frac{\partial c_h}{\partial t} v_h d\Omega + \int_\Omega D\nabla c_h \cdot \nabla v_h d\Omega = \int_\Omega \phi v_h d\Omega \quad \forall v_h \in V_h \end{cases} \tag{2.30}$$

It is sufficient that the Equation 2.30 is valid for the element of basis of the test functions subspace V_h and writing c_h as a linear combination of the vector basis $\varphi_j(x,y,z)$:

$$\int_\Omega \sum_{i=1}^{n} (\dot{c}_i(t)\varphi_i)\varphi_j d\Omega + \int_\Omega D \sum_{i=1}^{n} (c_i(t)\nabla\varphi_i)\cdot\nabla\varphi_j d\Omega = \int_\Omega \phi\varphi_j d\Omega \quad \forall j = 1,...,n \tag{2.31}$$

Due to linearity of summation and integral and considering that $c_i(t)$ and $\dot{c}_i(t)$ are just time dependent because the space dependency is linked to the shape functions:

$$\sum_{i=1}^{n} \dot{c}_i(t) \int_\Omega \varphi_i\varphi_j d\Omega + \sum_{i=1}^{n} c_i(t) \int_\Omega D\nabla\varphi_i\cdot\nabla\varphi_j d\Omega = \int_\Omega \phi\varphi_j d\Omega \quad \forall j = 1,...,n \tag{2.32}$$

Therefore, the j-th equation can be written in the following matrix form:

$$[b_{j1}\ \cdots\ b_{ji}\ \cdots\ b_{jn}] \begin{bmatrix} \dot{c}_1(t) \\ \vdots \\ \dot{c}_i(t) \\ \vdots \\ \dot{c}_n(t) \end{bmatrix} + [a_{j1}\ \cdots\ a_{ji}\ \cdots\ a_{jn}] \begin{bmatrix} c_1(t) \\ \vdots \\ c_i(t) \\ \vdots \\ c_n(t) \end{bmatrix} = b_j \tag{2.33}$$

whose elements are reported in Equation 2.34.

$$b_{ji} = \int_\Omega \varphi_i \varphi_j d\Omega \quad , \quad a_{ji} = \int_\Omega D\nabla\varphi_i \cdot \nabla\varphi_j d\Omega \quad , \quad f_j = \int_\Omega \phi\varphi_j d\Omega \tag{2.34}$$

The complete matrix form is obtained combining the n equations:

$$[B]\{\dot{c}\} + [A]\{c\} = \{f\} \tag{2.35}$$

2.3 Homogenization

In accurately modeling and understanding complex engineering and scientific problems it can be crucial accounting for the coupling of the physical phenomena across the different scales of the system. Systems often exhibit behavior that spans multiple spatial scales, meaning that small-scale phenomena can significantly influence large-scale behavior and vice versa. For example, in material science, the microscopic structure of a material (like grain boundaries in metals or the arrangement of fibers in a composite) can affect its macroscopic properties, such as strength, ductility, and thermal conductivity. In the context of multiphysics problems, coupling across scales ensures that interactions at different levels are properly accounted for.

The technique used to achieve macroscopic properties of a material from the microscopic behaviour of its constituents is called Homogenization. It is useful to extract homogeneous parameter of a material or a system from its heterogeneous repetitive or representative structure at a lower scale. It is very effective in reducing the simulation time of complex multi-scale analysis because it makes not necessary the detailed complex geometry of the whole system.

The homogenization method can be divided into two main groups: analytical and numerical. In both of them there is the need of extracting a Representative Volume Element (RVE) of the system in order to achieve homogenized properties accounting for the heterogeneity of the system in its lower scales.

2.3.1 Analytical homogenization

The homogenization analytical methods are also called "rule of mixture". The macroscopic homogenized properties are evaluated from the microscopic constituents properties weighted by their volume fraction in the Representative Volume Element (RVE).

The simplest analytical method is the Volume Average model: the generic effective macroscopic property X is the weighted average of the constituents corresponding property X_i and the weights are the volume fractions $v_{f,i}$. With n isotropic constituents:

$$X = \sum_{i=1}^{n} v_{f,i} X_i \tag{2.36}$$

This model fits very well with isotropic materials. Although, when dealing with composite and more complex materials, direction-dependent properties are very common. In this case, ad hoc model can be developed. For instance, the Voigt-Reuss model [30, 31] fits very well with continuous orthotropic fibers embedded in an isotropic matrix. It is based on equilibrium and compatibility equations when a unidirectional fiber RVE (Figure 2.6) is under certain loading conditions along its material principal axis: 1 (parallel to the fibers), 2 (in-plane orthogonal to the fibers) and 3 (out-of-plane orthogonal to the fibers). This is true under the assumption of the "slab" model RVE: the volume fraction is equal to the surface and the width fractions. In general, the Voigt-Reuss model results with n constituents are:

$$E_{11} = \sum_{i=1}^{n} v_{f,i} E_{i,11} \tag{2.37}$$

$$E_{jj} = \sum_{i=1}^{n} \left(\frac{v_{f,i}}{E_{i,jj}}\right)^{-1} \tag{2.38}$$

$$G_{jk} = \sum_{i=1}^{n} \left(\frac{v_{f,i}}{G_{i,jk}}\right)^{-1} \tag{2.39}$$

$$\nu_{jk} = \sum_{i=1}^{n} v_{f,i} \nu_{i,jk} \tag{2.40}$$

As already said, this simple model works very well with unidirectional fibers and in particular with just two constituents (the matrix and one fiber material oriented in the local 1-direction). Although, due to the slab RVE hypothesis, Voigt-Reuss model often needs corrections: other analytical model, more complex and complete, have been developed to be more accurate during the homogenization. Some of those are Halpin-Tsai, Halpin-Tsi-Nielsen and Hashin-Rosen models [32].

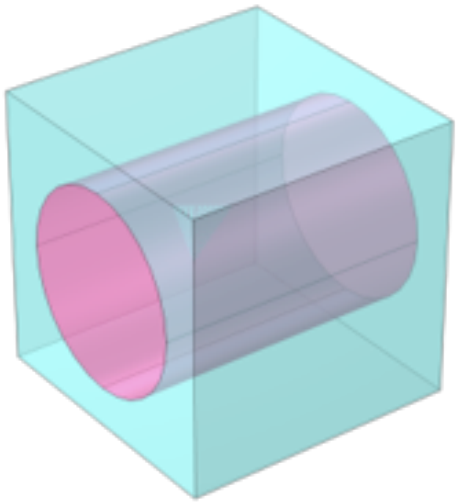

Fig. 2.6 Example of unidirectional fiber RVE

2.3.2 Numerical homogenization

With the increasing complexity at the microscale, analytical methods can be very complex or they can lead to inaccurate results. Another way to perform homogenized properties at the macroscale is numerically. One of the numerical approach is the finite element homogenization: it briefly consists in extracting material properties applying the finite element method - with the proper load cases and boundary conditions - to a Representative Volume Element (RVE) or a Repeating Unit Cell (RUC) of the system. The difference between the two stands in the boundary conditions because the latter is characterized by periodicity and the former is just a representative volume.

The objective is to obtain the stiffness matrix numerically. This is possible imposing an averaged strain and evaluating the corresponding induced stress as shown in Figure 2.7. In the most general case - a 3D anisotropic homogenization - six load cases are needed: three normal strains and three shear strains decoupled:

$$\begin{Bmatrix} \varepsilon_{avg,11} \\ 0 \\ 0 \\ 0 \\ 0 \\ 0 \end{Bmatrix} \begin{Bmatrix} 0 \\ \varepsilon_{avg,22} \\ 0 \\ 0 \\ 0 \\ 0 \end{Bmatrix} \begin{Bmatrix} 0 \\ 0 \\ \varepsilon_{avg,33} \\ 0 \\ 0 \\ 0 \end{Bmatrix} \begin{Bmatrix} 0 \\ 0 \\ 0 \\ \varepsilon_{avg,12} \\ 0 \\ 0 \end{Bmatrix} \begin{Bmatrix} 0 \\ 0 \\ 0 \\ 0 \\ \varepsilon_{avg,23} \\ 0 \end{Bmatrix} \begin{Bmatrix} 0 \\ 0 \\ 0 \\ 0 \\ 0 \\ \varepsilon_{avg,31} \end{Bmatrix}$$

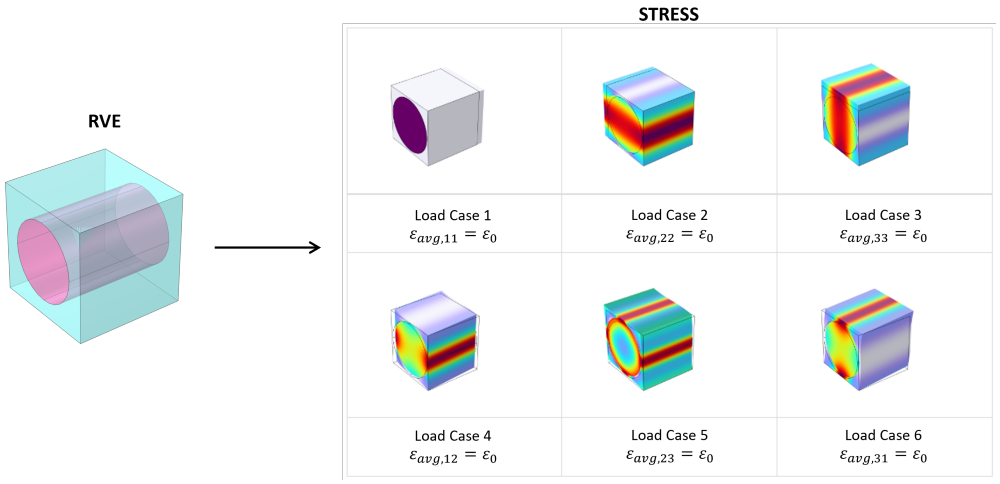

Fig. 2.7 Homogenization load cases

For each load case, the six corresponding stress can be averaged inside the representative volume element to obtain a single homogenized value for each vector component (Equation 2.41). Finally, the elements of the homogenized stiffness matrix can be computed as the ratio between the averaged stress and the imposed strain as shown in Equation 2.42.

$$\begin{Bmatrix} \sigma_{avg,11}(\varepsilon_{avg,ij}) \\ \sigma_{avg,22}(\varepsilon_{avg,ij}) \\ \sigma_{avg,33}(\varepsilon_{avg,ij}) \\ \sigma_{avg,12}(\varepsilon_{avg,ij}) \\ \sigma_{avg,23}(\varepsilon_{avg,ij}) \\ \sigma_{avg,31}(\varepsilon_{avg,ij}) \end{Bmatrix} \quad \forall i,j \in \{1,2,3\} \tag{2.41}$$

$$D_{ij} = \frac{\sigma_i(\varepsilon_j)}{\varepsilon_j} \quad \forall i,j \in \{1,\ldots,6\} \tag{2.42}$$

It can also be done imposing the stress, measuring the strain and computing the homogenized compliance matrix resulting in Equation 2.44. Also a free expansion can be imposed to evaluate the thermal expansion or the hygroscopic swelling coefficients.

$$\begin{Bmatrix} \sigma_{avg,11} \\ \sigma_{avg,22} \\ \sigma_{avg,33} \\ \sigma_{avg,12} \\ \sigma_{avg,23} \\ \sigma_{avg,31} \end{Bmatrix} = D_{avg} \begin{Bmatrix} \varepsilon_{avg,11} \\ \varepsilon_{avg,22} \\ \varepsilon_{avg,33} \\ \varepsilon_{avg,12} \\ \varepsilon_{avg,23} \\ \varepsilon_{avg,31} \end{Bmatrix} \tag{2.43}$$

$$\begin{Bmatrix} \varepsilon_{avg,11} \\ \varepsilon_{avg,22} \\ \varepsilon_{avg,33} \\ \varepsilon_{avg,12} \\ \varepsilon_{avg,23} \\ \varepsilon_{avg,31} \end{Bmatrix} = S_{avg} \begin{Bmatrix} \sigma_{avg,11} \\ \sigma_{avg,22} \\ \sigma_{avg,33} \\ \sigma_{avg,12} \\ \sigma_{avg,23} \\ \sigma_{avg,31} \end{Bmatrix} \tag{2.44}$$

Being a representative or a repeating volume, there should be Boundary Pairs to be specified: in a three-dimensional simulation, the three pairs will identify the reference frame. It is necessary to make the software know the directions of the load cases.

The boundary conditions are different if the analyzed volume is a RVE (homogenous properties) or a RUC (periodic properties). The corresponding boundary conditions are the following:

- Imposing a RVE average strain, the displacement u is consequently imposed depending on the points position r

$$u = \varepsilon_{avg} r \tag{2.45}$$

- Imposing a RVE average stress, the traction T is consequently imposed depending on the points position

$$T = \sigma_{avg} n \tag{2.46}$$

- Imposing a RUC average strain or stress, the displacement field - in both cases - has a periodic expression

$$u_{dst} = u_{src} + \varepsilon_{avg}(r_{dst} - r_{src}) \tag{2.47}$$

  where *dst* stands for *destination* and *src* stands for *source*.

Chapter 3

Modelling of Lithium-Ion Batteries

3.1 Introduction to lithium-ion batteries modelling

Lithium-ion battery modelling has emerged as a critical field of study to understand, predict, and optimize the behavior of batteries under various operational conditions. As lithium-ion batteries power an increasing number of technologies, ranging from electric vehicles to grid-scale energy storage systems, accurate and efficient models are essential for improving battery performance, safety, and longevity.

The primary objective of lithium-ion battery modeling is to capture the complex electrochemical, thermal, and mechanical processes that occur within the battery. These processes are highly interconnected and vary over different time scales, making the development of accurate models a challenging task. Through modeling, researchers and engineers aim to simulate battery behavior under different operating scenarios without the need for exhaustive physical testing, reducing both time and cost in battery development.

Models also allow the exploration of degradation mechanisms, thermal runaway risks, and capacity fade, all of which are crucial to improving the safety and durability of lithium-ion batteries. Furthermore, with the increasing focus on fast-charging and high-power applications, advanced models are required to account for the nonlinearities and dynamic behavior of the battery during extreme conditions.

3.1.1 Scope and Relevance

The importance of battery modeling lies in its ability to support several key areas of battery research and application.

- Design Optimization: By simulating the effects of material properties, geometries, and operating conditions, models can inform the design of batteries with enhanced energy density, power output, and thermal management. This significantly reduces the time and cost associated with experimental prototyping.
- Battery Management Systems (BMS): Accurate models are essential for the development of advanced BMS that can monitor, control, and optimize battery operation in real-time. The ability to predict state-of-charge (SOC), state-of-health (SOH), and temperature allows for better control over charge/discharge cycles, improving both performance and safety.
- Degradation Analysis: Modeling provides insight into aging mechanisms such as capacity fade and impedance rise. By predicting how batteries degrade over time under different cycling conditions, models can be used to extend battery life and develop more robust operational strategies.
- Thermal Management: Thermal effects have a significant impact on battery performance and safety, particularly in high-power applications. Models that accurately predict heat generation and dissipation help in the design of effective cooling strategies, reducing the risk of overheating and thermal runaway.
- Fast Charging: As demand for fast-charging solutions grows, models are used to analyze and mitigate the impact of high charge rates on battery life and safety. Through simulation, optimal charging protocols can be designed to minimize degradation while still meeting performance requirements.

3.1.2 Types of Model

There are several approaches to modeling lithium-ion batteries, each differing in complexity, computational cost, and the specific phenomena they aim to capture. The three most common categories are equivalent circuit models (ECMs), empirical models, and physics-based models.

- Equivalent Circuit Models (ECM): ECMs are widely used due to their simplicity and computational efficiency. They represent the battery as a network of electrical components, such as resistors and capacitors, that mimic the dynamic behavior of the battery. While ECMs can provide good approximations of battery voltage response and are effective for battery management systems (BMS), they fall short in capturing internal physical and chemical phenomena, making them less accurate for predicting long-term degradation and performances under different case scenarios [33].

- Empirical Models: Empirical models use data-driven approaches to predict battery behavior. These models rely on large datasets obtained from experiments to derive mathematical relationships between inputs (e.g., temperature, current, and state of charge) and outputs (e.g., voltage, capacity, and lifetime). Although they can offer high accuracy over specific conditions, empirical models lack the possibility to generalize to new operating regimes or cell chemistries and may require frequent recalibration based on continuous data collection.

- Physics-Based Models (Electrochemical Models): The most detailed and accurate form of battery modeling comes from physics-based approaches, which are derived from fundamental electrochemical, thermodynamic and mechanical principles. These models, such as the Doyle-Fuller-Newman (DFN) model [34, 35], explicitly simulate the internal dynamics of lithium-ion transport, intercalation reactions, and thermal effects inside the cell. Physics-based models provide deep insights into the operation and degradation mechanisms of the battery but often come with high computational cost and complexity. For this reason, they are commonly used in research and optimization rather than real-time applications.

The electrochemical processes which allow the battery to store and release electrical energy involve the interaction of lithium ions with the electrode microstructure causing its mechanical deformation. Therefore, analyze both the electrochemical and the mechanical model and then their interplay role inside the battery is crucial for the safe-optimization of the system.

In this work, aiming to capture the multiphysics aspect of the battery system, one of the most common physics-based model is presented in the following paragraphs.

Unlike simplified models, which focus primarily on electrical characteristics, a physics-based approach enables a detailed simulation of the complex interactions between electrochemical, thermal, and mechanical phenomena within the battery. By incorporating fundamental equations governing ion transport, electrode reactions, and elasticity equations, the electrochemical and mechanical models and their interplay - shown in the next paragraphs - could provide a comprehensive understanding of the battery's performance, degradation, and behavior under various operational conditions. Such an approach is essential for accurately predicting battery dynamics and optimizing its design and management strategies.

3.2 Doyle-Fuller-Newman model

At the core of a lithium-ion battery's function is its electrochemical model, which describes how energy is stored and released through the movement of lithium ions. The diffusion of lithium-ions and its consequences should be analyzed at two different scale and then study their coupling. In this section, the DFN model is deeply investigated.

3.2.1 Particle scale

Due to lithium ions migration between the two electrodes, there should be a moment in which the surface of the active material particle and its core are characterized by two different amount of concentration. The lithium ions concentration field can be described by the Fick's laws.

The first Fick's law describes the diffusion processes highlighting that a generic particles flux J is proportional to the particles concentration gradient ∇c flowing from high-concentration areas to low-concentration ones. The proportionality is given by the diffusion coefficient (or diffusivity) D. In a 1D problem, the equation is the following:

$$J = -D\frac{\partial c}{\partial x} \tag{3.1}$$

The second Fick's law is the application of the mass conservation to the diffusive processes. At the particle level, it is described by the Equation 2.20 without the source term because there is no internal generation of lithium ions: the variation of the analyzed species concentration in time is balanced by the net ions flux inside the analyzed system as shown in Equation 3.2. In a 1D diffusive problem, it is simplified in Equation 3.3.

$$\frac{\partial c}{\partial t} = \nabla \cdot (D \nabla c) \tag{3.2}$$

$$\frac{\partial c}{\partial t} = D \frac{\partial^2 c}{\partial x^2} \tag{3.3}$$

Applying this model to active material particles and making the assumption of isotropic spherical geometry, the second Fick's law can be expressed in spherical coordinates:

$$\frac{\partial c_s(z,r,t)}{\partial t} = \frac{D_s}{r^2} \frac{\partial}{\partial r} (r^2 \frac{\partial c_s(z,r,t)}{\partial r}) \tag{3.4}$$

The concentration in the solid phase c_s depends on time, on the radial coordinate r of the active material particle - due to the mentioned concentration gradient - and on the z coordinate of the electrodes due to non homogeneous distribution of lithium ions. In fact, during the operating conditions, the "in-charge" electrode presents higher concentration close to the separator and vice versa because those are the areas with the less-constrained ions. The same behaviour is seen at the particle level because the core lithium ions are more constrained (Figure 3.1) then the ones on the surface. This model is also called *pseudo-two-dimensional* (P2D) model because it is applied in a mono-dimensional domain but with a second dimension distribution - represented by the particle radius - at each point. A complete schematization of the P2D model is following presented in Figure 3.2

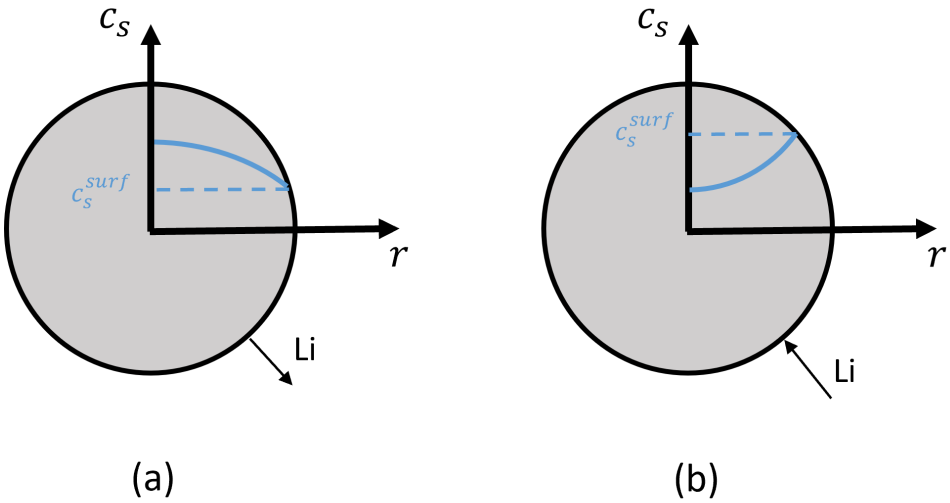

Fig. 3.1 Particle concentration field during (a) delithiation and (b) lithiation

3.2.2 Electrode scale

There is another crucial mass balance equation to be considered in the model. In this case, it is applied to the salt concentration in the electrolyte, denoted as c_l, at the electrode scale.

$$\varepsilon_l \frac{\partial c_l(z,t)}{\partial t} = \frac{\partial}{\partial z}(\varepsilon_l D_l^H \frac{\partial c_l(z,t)}{\partial z}) + a_s(1-t_+)J_{Li}(z,t) \tag{3.5}$$

The difference from Equation 3.3 stands in the presence of an additional sink/source term due to lithium insertion/deinsertion in/from the active material particles. This term contains the lithium ions flux J_{Li}, the particles active surface area per unit electrode volume a_s and the tranference number t_+ which is a measure of the fraction of the total ionic current in an electrolyte that is carried by lithium ions. Additionally, ε_l is the electrode porosity which is very close to its liquid phase fraction and D_l^H is the homogenized diffusivity of the electrolyte.

The two mass balance equations can be considered the chemical part of the electrochemical model. They describe the diffusion processes and how a species concentration can vary inside a domain. Instead, the electrical side in mainly described by two current conservation equations, both at solid and electrolyte phases.

They introduce two crucial parameters representing the active material (solid) and the electrolyte (liquid) potentials, Φ_s and Φ_l respectively.

$$\kappa_s^H \frac{\partial^2 \Phi_s}{\partial z^2} = a_s i(z,t) \tag{3.6}$$

$$\frac{\partial}{\partial z}[\kappa_l^H (\frac{\partial \Phi_l}{\partial z} - \frac{2RT}{F}(1 + \frac{\partial ln(f)}{\partial ln(c_l)})(1 - t_+)\frac{\partial ln(c_l)}{\partial z})] = -a_s i(z,t) \tag{3.7}$$

The right-sides of the Equations 3.6 and 3.7 are obviously the same but with opposite sign. The term $i(z,t)$ is the current density between the solid and the electrolyte interface. Knowing that the Faraday constant F is representative of the charge inside an electrons mole ($F = 96485\ C/mol$) and that stoichiometrically, in the lithium RED-OX, the molar ratio between Li^+ and e^- is 1:1, $i(z,t)$ can be expressed as:

$$i(z,t) = F J_{Li,k}(z,t) \tag{3.8}$$

On the other side, κ_s^H and κ_l^H are the homogenized electrical conductivity of the solid phase and the electrolyte respectively. The homogenized conductivities and electrolyte diffusivity of the composite electrodes and separator can be evaluated accounting for porosity ε and tortuosity τ inside the corresponding domains. Equations 3.9 and 3.10 highlight these dependencies.

$$\kappa^H = \frac{\varepsilon}{\tau}\kappa \tag{3.9}$$

$$D^H = \frac{\varepsilon}{\tau} D \tag{3.10}$$

Tortuosity and porosity are usually related by the Bruggeman relation, which leads to the corresponding corrections [36].

$$\kappa_s^H = \kappa_s \varepsilon_l^{brugg} \tag{3.11}$$

$$\kappa_l^H = \kappa_l \varepsilon_l^{brugg} \tag{3.12}$$

$$D_l^H = D_l \varepsilon_l^{brugg} \tag{3.13}$$

The coefficient *brugg* is obtained fitting the corresponding property trend and it usually is 1.5 or 4.5.

3.2.3 Electrochemical coupling across scales

The general lithium intercalation or deintercalation reaction in the electrode can be written as:

$$Li - \Theta \rightleftharpoons Li^+ + e^- + \Theta \tag{3.14}$$

where Θ represents the intercalation site in the electrode solid, and $Li - \Theta$ represents the lithium in the electrode solid.

The Reaction 3.14 can proceed in both direction, forward and backward representing an anodic and a cathodic reaction respectively. The rate at which the forward and backward reactions occur depends on the overpotential (η), which is the difference between the electrode potential and the equilibrium one.

$$\eta(z,t) = \Phi_s(z,t) - \Phi_l(z,t) - E_{ref} \tag{3.15}$$

Precisely, the rate of the electrochemical reaction depends exponentially on the overpotential due to the Boltzmann factor, which reflects the probability that molecules have enough energy to overcome the activation threshold. The anodic and cathodic current densities are therefore expressed as:

$$i_a(z,t) = i_0(z,t) \cdot exp(\frac{\alpha_a F \eta(z,t)}{R_g T}) \tag{3.16}$$

$$i_c(z,t) = i_0(z,t) \cdot exp(\frac{-\alpha_c F \eta(z,t)}{R_g T}) \tag{3.17}$$

where α_a and α_c are the anodic and cathodic charge transfer coefficients, two parameters indicating how much the overpotential contributes to driving the anodic

or cathodic reaction respectively. In fact, $\alpha_i F \eta(z,t)$ is the equivalent anodic or cathodic activation energy. The charge transfer coefficients are usually connected by the following relation:

$$\alpha_a + \alpha_c = 1 \tag{3.18}$$

so that $\alpha_a = \alpha$ and $\alpha_c = 1 - \alpha$ or vice versa.

The net current density at the electrode $i(z,t)$ is the difference between the anodic current density and the cathodic one, resulting in the Butler-Volmer equation:

$$i(z,t) = i_0(z,t)(exp(\frac{\alpha F \eta(z,t)}{RT} - exp(\frac{-(1-\alpha)F\eta(z,t)}{RT})) \tag{3.19}$$

Additionally, $i_0(z,t)$ is the equilibrium current density, for $\eta = 0$. In a generic RED-OX, it can be expressed as:

$$i_0 = nFk(c_{red}^{\alpha_c} c_{ox}^{\alpha_a}) \tag{3.20}$$

where n is the number of the electrons involved in the reaction, k is the reaction rate, c_{red} and c_{ox} are the concentration of the reducted and oxidized species at the electrode surface. The Equation 3.20 applied to the Reaction 3.14, where the reduced/oxidized species is the lithium and $n = 1$, result in:

$$i_0(z,t) = Fk(c_{s,surf}(z,t))^{1-\alpha}(c_{s,max} - c_{s,surf}(z,t))^{\alpha} c_l^{\alpha}(z,t) \tag{3.21}$$

because the reduced lithium is the one in the electrode solid, represented by the backward reaction (cathodic) and the oxidized one is present in the electrolyte represented by the forward reaction (anodic). $(c_{s,max} - c_{s,surf}(z,t))^{\alpha}$ is a driving force term because there is a limit of lithium concentration inside the active particle material: when $c_{s,surf} = c_{s,max}$ there is no concentration gradient that makes the anodic reaction proceed. The exchange current density is higher when the gradient inside the particles is higher. Usually the charge transfer coefficients are the same: $\alpha_a = \alpha_c = \alpha = 0.5$.

$$i_0(z,t) = Fk[c_{s,surf}(z,t)c_l(z,t)(c_{s,max} - c_{s,surf}(z,t)]^{0.5} \tag{3.22}$$

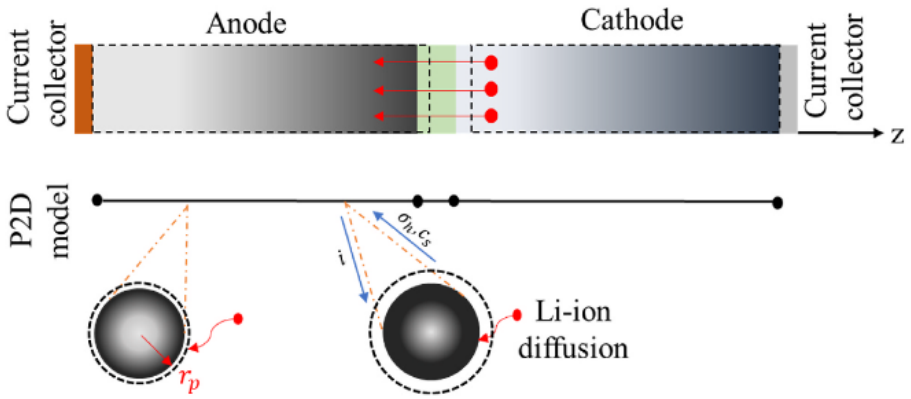

Fig. 3.2 P2D model - Concentration field at particle and electrode levels [20]

3.3 Mechanical model

The mechanical behavior of lithium-ion batteries is a critical aspect that significantly influences their performance, safety, and lifespan. While electrochemical processes are central to battery operation, the mechanical stresses and strains that occur during these processes are equally important. As lithium ions intercalate and deintercalate from the electrode materials, the electrodes undergo volumetric changes, leading to mechanical deformation. This can cause various issues, such as cracking and capacity fade, which degrade the battery's overall performance.

3.3.1 Atomic scale

The active materials are responsible for hosting the lithium ions during the charge and discharge processes, acting as storage mediums for lithium ions that move between the electrodes. Therefore, the lattice structure is crucial for the evaluation of the mechanical consequences induced from the electrochemical process: during lithiation - and consequenly during the lithium ions hosting - the lattice structure goes under deformation and/or arrangement variation.

The partial molar volume Ω is defined as the volume change induced to the hosting material by the addition of one mole of solute. In general, the partial molar volume can be defined as the variation of volume due to solute insertion V^m with respect to the corresponding moles of solute n. Considering that the molar volume

can be expressed as function of the initial molar volume V_0^m and the deformation of the crystal lattice structure ε_v^c:

$$\Omega = \frac{\partial V^m}{\partial n} = V_0^m \frac{\partial \varepsilon_v^c}{\partial n} \tag{3.23}$$

Therefore, measuring the volumetric strain of the crystal lattice structure from XRD analysis, the partial molar volume can be computed.

It is not obvious that it is a constant coefficient. In fact - as already said - during lithiation, the lattice structure can vary its atomic arrangement and change its response to deformation. It can be generally said that the partial molar volume is function of the lithium ions concentration in the hosting material. In particular, defining $c_{s,max}$ as the maximum amount of lithium ions concentration, a state of lithiation *sol* can be defined as the ratio between the actual concentration and the maximum one in both the electrodes:

$$x = \frac{c_s^{an}}{c_{s,max}^{an}} \quad y = \frac{c_s^{cat}}{c_{s,max}^{cat}} \tag{3.24}$$

$$0 \leq x, y \leq 1$$

where x is the anode state of lithiation (e.g Li_xC_6 for graphite) and y is the cathode one (e.g Li_yFePO_4 for LFP and Li_yCoO_2 for LCO). The partial molar volume is dependent on the state of lithiation x and y.

As shown in Figure 3.3b, LFP is characterized by a constant partial molar volume and consequently linear strain [37]. More interesting is the graphite behaviour that undergoes atomic structure variation due to lithiation and exhibits a step behaviour of $\Omega_{graph}(x)$ (Figure 3.3a). The dependency is not only on the state of lithiation but also on current rates.

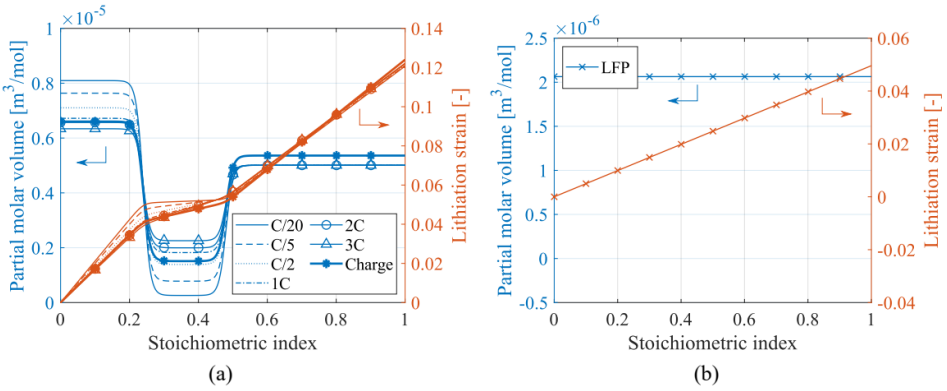

Fig. 3.3 Partial molar volume and lithiation strain of (a) graphite and (b) LFP

In the lithiation window of graphite can be identified five main crystal stages characterized by their own lattice parameters: the in-plane spacing between carbon atoms d_{cc} and the carbon layer spacing d_l [38]. The layered structure of graphite is described in Paragraph 1.2.1 and shown in Figure 1.2a. The five stages and their comparison during lithiation/delithiation are schematized in Figure 3.4: the solid lines are the carbon planes and the dashed ones are the lithium ions inserted.

It can be notices that during lithiation of graphite - therefore during the battery charge - the IIL stage is skipped. The presence of the IIL stage is not only dependent on the current direction but also on temperature and discharging rate, that is the reason of the C-rate dependency of the graphite partial molar volume during discharging [39]. In particular, stage IIL of graphite appears at low discharge rates.

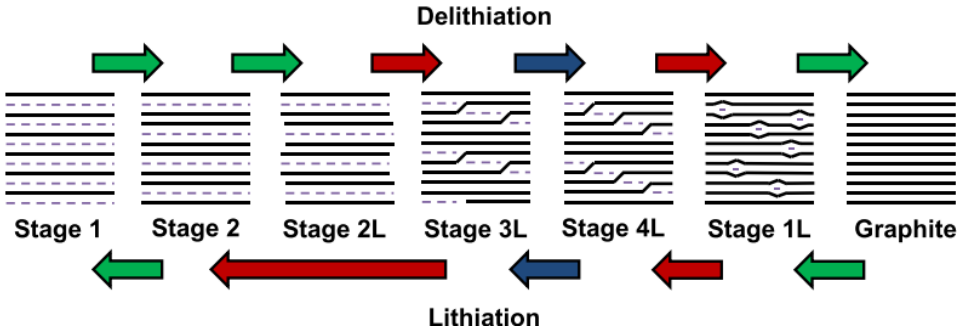

Fig. 3.4 Graphite stages during lithiation and delithiation [38]

3.3.2 Particle scale

Due to the symmetry of the system - assuming spherical particles - the principal reference frame of the single particle is represented by a radial and two hoop coordinates. Therefore, the structural mechanics set of PDEs can be expressed as following:

- Compatibility equations

$$\varepsilon_r = \frac{du}{dr} \tag{3.25}$$

$$\varepsilon_c = \frac{u}{r} \tag{3.26}$$

- Equilibrium equation

$$\frac{d\sigma_r}{dr} + \frac{2}{r}(\sigma_r - \sigma_c) = 0 \tag{3.27}$$

- Constitutive laws

$$\varepsilon_r^{mec} = \frac{1}{E}(\sigma_r - 2\nu\sigma_c) \tag{3.28}$$

$$\varepsilon_c^{mec} = \frac{1}{E}((1-\nu)\sigma_c - \nu\sigma_r) \tag{3.29}$$

Lithium intercalation and deintercalation induce swelling and shrinking in the particle of the active material. Due to spherical geometry hypothesis, this deformation is isotropic and assumed to be elastic. The particle swelling/shrinking due to lithium intercalation/deintercalation can be modeled as a thermal or hygroscopic volumetric deformation. In this case, the volumetric strain is proportional to the difference between the actual lithium ion concentration and the initial state one through the partial molar volume.

$$\varepsilon_v^{ch} = \Omega(c_s - c_{s,0}) \tag{3.30}$$

As shown in the previous paragraph, the partial molar volume can depend on the state of lithiation and - consequently - on the lithium ions concentrations. Therefore, the differential form of the chemical volumetric strain is necessary (Equation 3.31). However, for the following computations, a constant partial molar volume is assumed.

$$d\varepsilon_v^{ch} = \Omega(c_s)dc_s \tag{3.31}$$

Due to the isotropic effect of the chemical deformation, the volumetric strain described in Equations 3.30 contributes both to the radial and the two hoop strain in the same way: the corresponding swelling/shrinking linear coefficient is a third of the partial molar volume. The radial and hoop strain, considering both the mechanical and chemical contribute, can therefore be written as:

$$\varepsilon_r = \frac{1}{E}(\sigma_r - 2\nu\sigma_c) + \frac{\Omega}{3}\tilde{c} \tag{3.32}$$

$$\varepsilon_c = \frac{1}{E}((1-\nu)\sigma_c - \nu\sigma_r) + \frac{\Omega}{3}\tilde{c} \tag{3.33}$$

where $\tilde{c}$ represent the difference in concentration that drive the chemical strain.

To compute the particle deformation $u(r)$, this set of equations can be managed as following [6]:

1. substitute the compatibility equations (3.25 and 3.26) in the corresponding constitutive laws (3.32 and 3.33);
2. compute σ_r and σ_c from the previous equations;
3. obtain a single second order differential equation substituting σ_r, σ_c and $\frac{d\sigma_r}{dr}$ in the equilibium equation (3.27);
4. integrate two times to obtain $u(r)$.

$$u(r) = \frac{\Omega}{3(1-\nu)}[(1+\nu)\frac{1}{r^2}\int_0^r \tilde{c}(r)r^2dr + 2(1-2\nu)\frac{r}{r_p^3}\int_0^{r_p} \tilde{c}(r)r^2dr] \tag{3.34}$$

The displacement of each point of the particle depends on the lithium concentration field inside the domain. This field derives from the diffusive problem described in Paragraph 3.2.1 highlighting one of the multyphisics aspects of the system. Additionally, the stress inside the particle affects the diffusive problem itself modifying the Fick's laws:

$$J_{Li} = -D(\frac{\partial c_s}{\partial r} - \frac{\Omega c_s}{RT}\frac{\partial \sigma_h}{\partial r}) \tag{3.35}$$

$$\frac{\partial c_s}{\partial t} = D_s[\frac{\partial^2 c_s}{\partial r^2} + \frac{2}{r}\frac{\partial c_s}{\partial r} - \frac{\Omega}{RT}\frac{\partial c_s}{\partial r}\frac{\partial \sigma_h}{\partial r} - \frac{\Omega c_s}{RT}(\frac{\partial^2 \sigma_h}{\partial r^2} + \frac{2}{r}\frac{\partial \sigma_h}{\partial r})] \tag{3.36}$$

The term σ_h is the hydrostatic stress and, mathematically, it is the average of the three principal stress:

$$\sigma_h = \frac{\sigma_1 + \sigma_2 + \sigma_3}{3} = \frac{\sigma_r + 2\sigma_c}{3} \tag{3.37}$$

Once computed $u(r)$, the expression of the radial stress, the hoop stress and, consequently, the hydrostatic stress can be obtained:

$$\sigma_r(r) = \frac{2\Omega E}{3(1-\nu)}(\frac{1}{r_p^3}\int_0^{r_p} \tilde{c}(r)r^2 dr - \frac{1}{r^3}\int_0^r \tilde{c}(r)r^2 dr) \tag{3.38}$$

$$\sigma_c(r) = \frac{\Omega E}{3(1-\nu)}(\frac{2}{r_p^3}\int_0^{r_p} \tilde{c}(r)r^2 dr + \frac{1}{r^3}\int_0^r \tilde{c}(r)r^2 dr - \tilde{c}(r)) \tag{3.39}$$

$$\sigma_h(r) = \frac{2\Omega E}{9(1-\nu)}(\frac{3}{r_p^3}\int_0^{r_p} \tilde{c}(r)r^2 dr - \tilde{c}(r)) \tag{3.40}$$

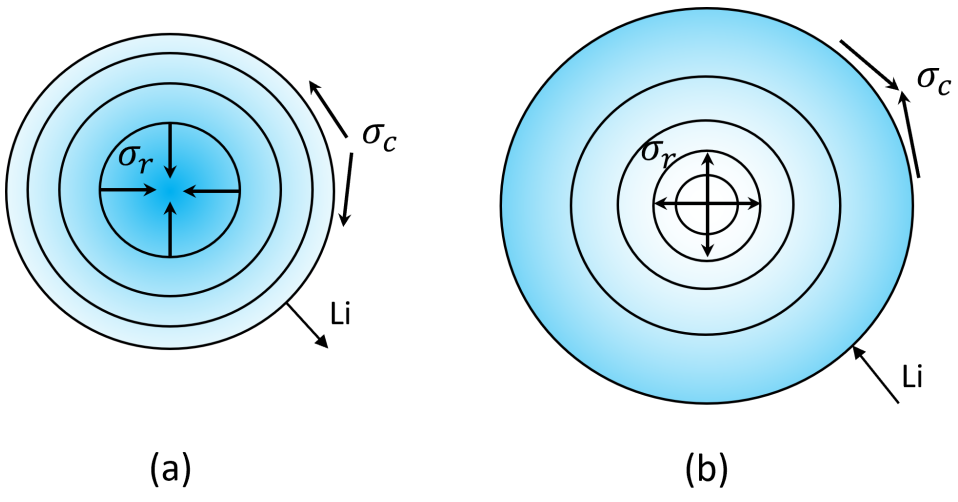

Fig. 3.5 Particle stress fields during (a) delithiation and (b) lithiation [40]

Equation 3.40 highlight the dependence of the hydrostatic stress from the lithium ions concentration. Therefore, Equation 3.35 can be simplified applying the chain rule $\frac{\partial \sigma_h}{\partial r} = \frac{\partial \sigma_h}{\partial c_s}\frac{\partial c_s}{\partial r}$ finding an equivalent diffusivity depending on the lithium ions concentration itself due to the stress state of the particle.

$$J = -D(1 + \frac{2\Omega^2 E c_s}{9RT(1-\nu)})\frac{\partial c_s}{\partial r} = -D_{eq}(c_s)\frac{\partial c_s}{\partial r} \tag{3.41}$$

Once the concentration field is known, the surface displacement can be computed replacing $r = r_p$ to Equation 3.34.

$$u(r = r_p) = \frac{\Omega}{r_p^2}\int_0^{r_p} \tilde{c}(r) r^2 dr = \frac{\Omega r_p}{3}(c_{s,avg} - c_{s,0}) \tag{3.42}$$

where $c_{s,avg}$ is the instantaneous mean concentration in the particle evaluated as:

$$c_{s,avg} = \frac{3}{r_p^3}\int_0^{r_p} c_s r^2 dr \tag{3.43}$$

The volumetric strain of the particle is analytically computed in the Equation 3.44 as the ratio between the variation in volume and the initial volume of the particle itself.

$$\varepsilon_v^p = \frac{\Delta V^p}{V_0^p} = \frac{\frac{4}{3}\pi((r_p + u(r_p))^3 - r_p^3)}{\frac{4}{3}\pi r_p^3} = \frac{3r_p^2 u(r_p) + 3r_p u^2(r_p) + u^3(r_p)}{r_p^3} \tag{3.44}$$

Due to small deformations, $u(r_p) \to 0$ and $\varepsilon_v^p \approx 3\frac{u(r_p)}{r_p}$.

3.3.3 Electrode scale

At the scale of the electrode, active material is one of the component of the composite structure, then it is important to understand the effect of the deformation of its particles on the electrode layer. Two primary effects can be expected: deformation of the overall electrode layer and a decrease in its porosity. Considering these two aspects, the electrode volume change ΔV^e can be expressed as the n^p active material

particles volume change corrected by the volumetric expansion parameter g which accounts for the porosity variation. This result is shown in Equation 3.45 [41].

$$\Delta V^e = g n^p \Delta V^p \tag{3.45}$$

Dividing both sides of the above equation by the initial particle volume V_0^p and considering that the n^p particles constitute the solid fraction ζ of the active layer ($n^p V_0^p = \zeta V_0^e$), the electrode volumetric strain can be related to the particle one as presented in Equation 3.46.

$$\varepsilon_v^e(c_s) = g\zeta\varepsilon_v^p(c_s) \tag{3.46}$$

For a free expansion deformation, this relation is analytically powerful because g can be assumed equal to 1: this hypothesis is due to the absence of an external pressure that can significantly change the porosity of the electrode. It can be necessary to evaluate the external boundary conditions numerically.

Electrochemically, the stress state in the active material particles also influences the overpotential of the electrodes: in the coupled problem, the Equation 3.15 is modified accounting for the hydrostatic stress and the surface contact resistance R_c:

$$\eta(z,t) = \Phi_s(z,t) - \Phi_l(z,t) - E_{ref} - \frac{\Omega\sigma_h(z,t)}{F} - R_c i(z,t) \tag{3.47}$$

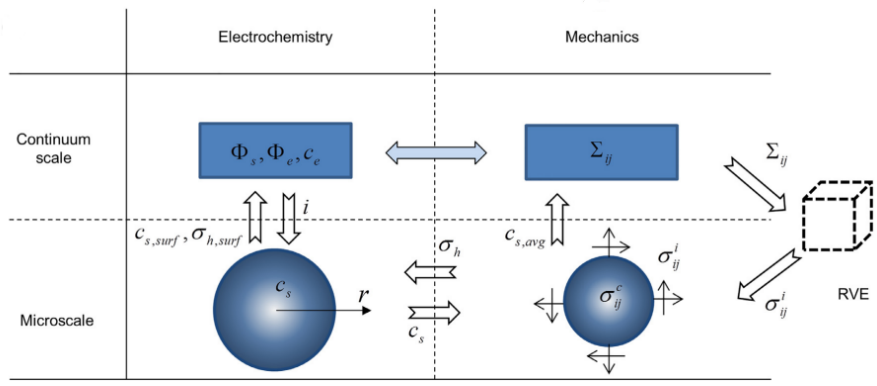

Fig. 3.6 Scheme of multi-scale and multi-physics coupling [42]

Chapter 4

Electrochemical-Mechanical Multiscale Battery Model

In this thesis, a comprehensive multi-scale model is developed to investigate the mechanical behavior of a battery module using COMSOL Multiphysics. The model is designed to perform structural analysis of a battery module accounting both for the mechanical consequences given by the internal electrochemical process and the external mechanical constraints during its operating conditions. The objective is to treat the batteries as homogeneous without the need of modelling the whole internal structure to perform cheaper simulations in terms of computational cost. The structural analysis performed in this work is focused on the battery module swelling during charging and the effect given by the spacing between the batteries. The model can be extended to all types of lithium-ion battery but an example of application is performed on a LFP/graphite battery module.

The use of COMSOL Multiphysics provides a versatile and powerful platform for coupling the various physical phenomena, ensuring a detailed and accurate representation of the battery's mechanical response under real-world conditions.

Using the Battery Design Module of COMSOL Multiphysics, the concentration of lithium ions within the electrode is computed through the physics-based electrochemical DFN model presented in the previous section. The concentration in the solid phase is the input of the mechanical model which consists on the analysis of the evolution of the deformation across the scales of the system. Due to the nano-

structured active materials and the amount of layers inside the battery, a two-step homogenization approach is followed.

4.1 Battery homogenization

The battery's intricate internal architecture - composed of several layers and nano-structured materials - present a unique challenge in numerical simulation: the direct modelling of every detail becomes impractical and computationally expensive. This challenge can be overcome by treating the active layers and the whole battery as homogenized materials. Once homogenized, the batteries or the entire battery module can be involved in more complex structural analysis.

The homogenization of periodic structures can be achieved efficiently through the *Cell Periodicity* in the Structural Mechanics Module of COMSOL Multiphysics. This function allows to simulate the mechanical behavior of periodic structures by modeling a representative volume rather than the entire structure. This significantly reduces computational complexity and time, especially for large, repeating systems like lattice structures or composites. In this work, the *Cell Periodicity* has been used to homogenize the active materials and the whole battery mechanical properties. In both cases it's about a Representative Volume Element and not a Repeating Unit Cell (see Paragraph 2.3).

Due to the small percentage of filler and conductive agents fraction, only the active material particles and the electrolyte have been considered as constituents of the active layer RVE which is represented by a Body-Centered Cube (BCC) due to particles arrangement (Figure 4.1). It is an isotropic RVE, then just a single normal strain load case is sufficient to extract the material parameters. This characteristic is easier to understand with the independent parameters of the compliance matrix $[S]$ in an isotropic case:

$$\begin{Bmatrix} \varepsilon_1 \\ \varepsilon_2 \\ \varepsilon_3 \\ \gamma_{23} \\ \gamma_{31} \\ \gamma_{12} \end{Bmatrix} = \begin{bmatrix} \frac{1}{E} & -\frac{\nu}{E} & -\frac{\nu}{E} & 0 & 0 & 0 \\ -\frac{\nu}{E} & \frac{1}{E} & -\frac{\nu}{E} & 0 & 0 & 0 \\ -\frac{\nu}{E} & -\frac{\nu}{E} & \frac{1}{E} & 0 & 0 & 0 \\ 0 & 0 & 0 & \frac{2(1+\nu)}{E} & 0 & 0 \\ 0 & 0 & 0 & 0 & \frac{2(1+\nu)}{E} & 0 \\ 0 & 0 & 0 & 0 & 0 & \frac{2(1+\nu)}{E} \end{bmatrix} \begin{Bmatrix} \sigma_1 \\ \sigma_2 \\ \sigma_3 \\ \tau_{23} \\ \tau_{31} \\ \tau_{12} \end{Bmatrix} \tag{4.1}$$

Thanks to the numerical homogenization approach - explained in Paragraph 2.3 - just applying one normal load case, the first row of the stiffness or compliance matrix can be obtained and consequently - in an isotropic case -the Young's modulus and the Poisson's ratio thanks to S_{11} and S_{12} (or D_{11} and D_{12}) .

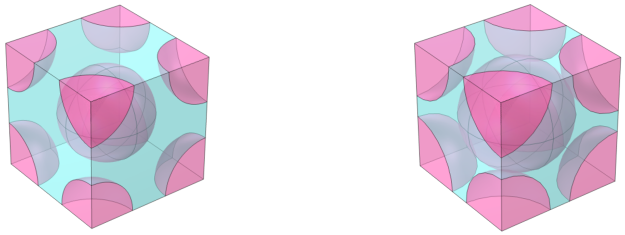

Fig. 4.1 (a) Anode and (b) cathode RVEs

The homogenized active layers are then part of the battery RVE which is represented by the following stack of thin layers:

- Copper cathode current collector
- Homogenized cathode active layer
- Separator
- Homogenized anode active layer
- Aluminum anode current collector

In this case, the resulting homogenized material results transversely isotropic because the in-plane directions are equal and the out-of-plane direction is different from them. This time, the independent parameters of the compliance matrix are five:

$$\begin{Bmatrix} \varepsilon_1 \\ \varepsilon_2 \\ \varepsilon_3 \\ \gamma_{23} \\ \gamma_{31} \\ \gamma_{12} \end{Bmatrix} = \begin{bmatrix} \frac{1}{E_1} & -\frac{\nu_{12}}{E_1} & -\frac{\nu_{12}}{E_1} & 0 & 0 & 0 \\ -\frac{\nu_{21}}{E_2} & \frac{1}{E_2} & -\frac{\nu_{23}}{E_2} & 0 & 0 & 0 \\ -\frac{\nu_{21}}{E_2} & -\frac{\nu_{23}}{E_2} & \frac{1}{E_2} & 0 & 0 & 0 \\ 0 & 0 & 0 & \frac{2(1+\nu_{23})}{E_2} & 0 & 0 \\ 0 & 0 & 0 & 0 & \frac{1}{G_{12}} & 0 \\ 0 & 0 & 0 & 0 & 0 & \frac{1}{G_{12}} \end{bmatrix} \begin{Bmatrix} \sigma_1 \\ \sigma_2 \\ \sigma_3 \\ \tau_{23} \\ \tau_{31} \\ \tau_{12} \end{Bmatrix} \tag{4.2}$$

in particular, the independent elastic parameters are the out-of plane Young's modulus E_1, the in-plane Young's modulus E_2, the major Poisson's ratio $\nu_{12} = \nu_{13}$, the in-plane Poisson's ratio ν_{23} and the shear modulus $G_{12} = G_{13}$. Due to the symmetry of the compliance matrix, the minor Poisson's ratio ν_{21} can be obtained from the major one the the two Young's modulus. Due to the in-plane isotropy, the in-plane shear modulus G_{23} depends just on the the corresponding Young's modulus and Poisson's ratio. It can be seen that - in this transversely isotropic case - the elements S_{11}, S_{12}, S_{22}, S_{23} and S_{55} (or D_{11}, D_{12}, D_{22}, D_{23} and D_{55}) are sufficient to evaluate all the independent elastic parameters. The same thing can be seen with the stiffness matrix and therefore, two normal strain load cases (one in-plane and one out-of-plane) and one out-of-plane shear strain load case are sufficient to entirely describe mechanically the RVE. A scheme of this two-homogenization procedure is shown in Figure 4.2.

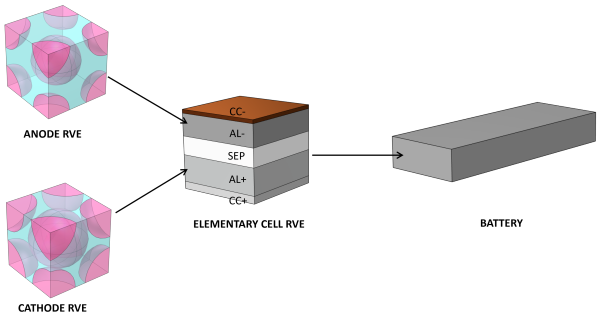

Fig. 4.2 Two-step homogenization

The output of the *Cell Periodicity* is a new custom material with the computed homogenized properties. For the LFP/graphite battery module the parameters reported in Table 4.1 are used: l from literature, m measured from SEM images (Figure 5.2), c calculated.

Table 4.1 Parameters for the LFP/graphite battery homogenization.

Domain	Property	Symbol	Value	Unit
Cathode Active Layer	Particle Young's Modulus	E_p^{cat}	125 $^{l[43]}$	GPa
	Particle Poisson's ratio	ν_p^{cat}	0.3 $^{l[43]}$	-
	Particle radius	r_p^{cat}	0.03 ^{m}	μm
	Porosity	ε_p^{cat}	0.608 ^{c}	-
	Thickness	t_{al}^{cat}	72 ^{m}	μm
Anode Active Layer	Particle Young's Modulus	E_p^{an}	15 $^{l[44]}$	GPa
	Particle Poisson's ratio	ν_p^{an}	0.3 $^{l[44]}$	-
	Particle radius	r_p^{an}	10 ^{m}	μm
	Porosity	ε_p^{an}	0.434 ^{c}	-
	Thickness	t_{al}^{an}	60 ^{m}	μm
Cathode Current Collector	Young's Modulus	E_{cc}^{cat}	70 ^{l}	GPa
	Poisson's ratio	ν_{cc}^{cat}	0.3 ^{l}	-
	Thickness	t_{cc}^{cat}	12 ^{m}	μm
Anode Current Collector	Young's Modulus	E_{cc}^{an}	110 ^{l}	GPa
	Poisson's ratio	ν_{cc}^{an}	0.3 ^{l}	-
	Thickness	t_{cc}^{an}	10 ^{m}	μm
Separator	Young's Modulus	E_{sep}	0.4 $^{l[45]}$	GPa
	Poisson's ratio	ν_{sep}	0.01 $^{l[45]}$	-
	Thickness	t_{sep}	33 ^{m}	μm

4.2 Electrochemical model

In COMSOL Multiphysics there are several Physics Module with their constitutive governing equations implemented. The Battery Design Module is a specialized tool used for simulating and analyzing battery systems. It enables researchers

and engineers to model the electrochemical, thermal and mechanical behaviors of batteries across various scales, from microscopic electrode structures to full battery packs. Supporting multiple battery chemistries like lithium-ion and lead-acid, the module allows for detailed studies on performance, efficiency, and safety, facilitating the design and optimization of advanced battery technologies.

In this work, the Battery Design Module has been applied to a 1D domain composed by the two active layers and the separator (Figure 4.3) in order to obtain the lithium ion concentration distribution across the electrodes thickness. The model can be generalized to all types of lithium-ion batteries but in this specific case, LFP/graphite batteries are analyzed. As shown in Figure 4.3, the origin of the domain is the cathode current collector for $z = 0$ while the end is the anode current collector for $z = t_{al}^{cat} + t_{sep} + t_{al}^{an} = L$.

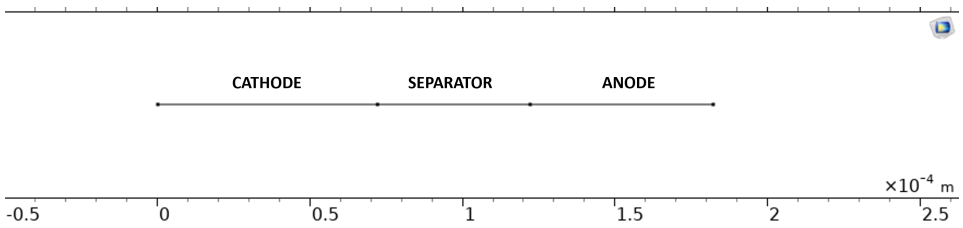

Fig. 4.3 Electrochemical model 1D domain

The implemented model is the DFN model, deeply described in Paragraph 3.2. In the following sections, the needed properties and boundary conditions are presented.

4.2.1 Materials and Properties

As shown in the previous chapter, the parameters that allows the computation of the DFN model are mainly related to the electrode composition and mechanical properties - already reported on Table 4.1 - and electrical and diffusive properties shown in Table 4.2 and in the next figures: l from literature, c calculated.

Table 4.2 Electrochemical model parameters

Property	Symbol	Cathode	Separator	Anode	Unit
Electrical properties					
Solid-phase conductivity	$\kappa_{s,k}$	6 $^{l[46]}$	-	100 $^{l[47]}$	S/m
Reaction rate	$k_{e,k}$	10^{-10} $^{l[46]}$	-	$5{\cdot}10^{-12}$ $^{l[46]}$	$m^{2.5}/mol^{0.5}s$
Contact resistance	$R_{c,k}$	0.05	-	0.05	Ωm^2
Diffusive properties					
Solid-phase diffusivity	$D_{s,k}$	$5.5{\cdot}10^{-19}$ $^{l[48]}$	-	Figure 4.4 $^{l[49]}$	m^2/s
Electrolyte diffusivity	$D_{l,k}$	$1.3{\cdot}10^{-10}$ $^{l[49]}$	$1.3{\cdot}10^{-10}$ $^{l[49]}$	$1.3{\cdot}10^{-10}$ $^{l[49]}$	m^2/s
Maximum Li-ion concentration	$c^k_{s,max}$	24035 ^{c}	-	26190 ^{c}	mol/m^3

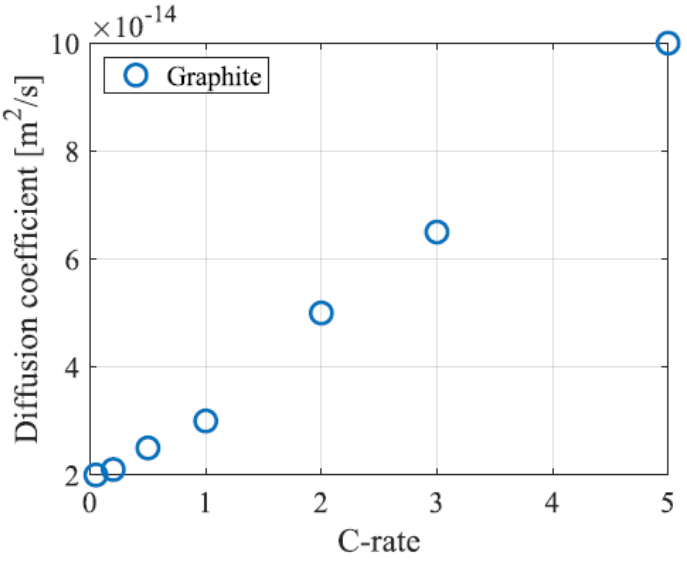

Fig. 4.4 Graphite diffusivity

The Open Circuit Potential (OCP) of the two electrodes are expressed in the following equations and plotted in the corresponding figures.

- Graphite [47]

$$
\begin{aligned}
U_{ref}^{Li_xC_6} = {} & 0.124 + 1.5(-150x) + 0.0155 \cdot tanh(\frac{x-0.205}{0.029}) \\
& - 0.011 \cdot tanh(\frac{x-0.124}{0.0226}) - 0.102 \cdot tanh(\frac{x-0.194}{0.142}) \\
& + 0.0347 \cdot tanh(\frac{x-0.286}{0.083}) - 0.0147 \cdot tanh(\frac{x-0.5}{0.034}) \\
& - 0.0045 \cdot tanh(\frac{x-0.9}{0.119}) - 0.022 \cdot tanh(\frac{x-0.98}{0.0164}) \\
& - 0.035 \cdot tanh(\frac{x-0.99}{0.05})
\end{aligned}
\tag{4.3}
$$

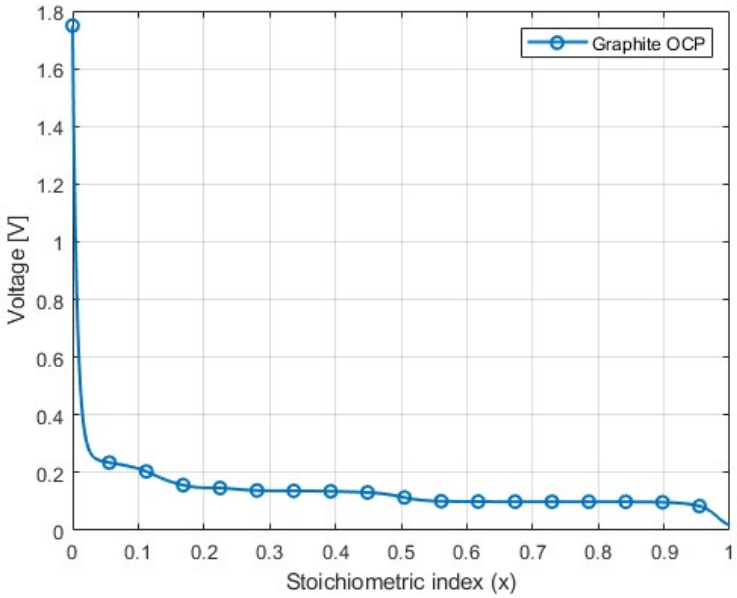

Fig. 4.5 Graphite OCP

- LFP [50]

$$
U_{ref}^{LFP} = 3.4245 + 2 \cdot exp(-800y^{1.3}) - 17 \cdot exp(-3.5/y^{14}) \tag{4.4}
$$

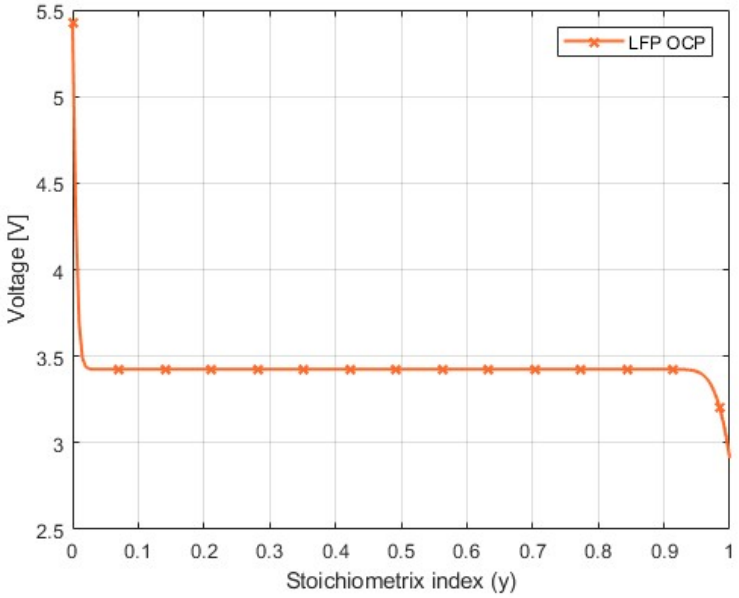

Fig. 4.6 LFP OCP

4.2.2 Boundary conditions

Figure 4.7 shows the used Battery Design Module model tree.

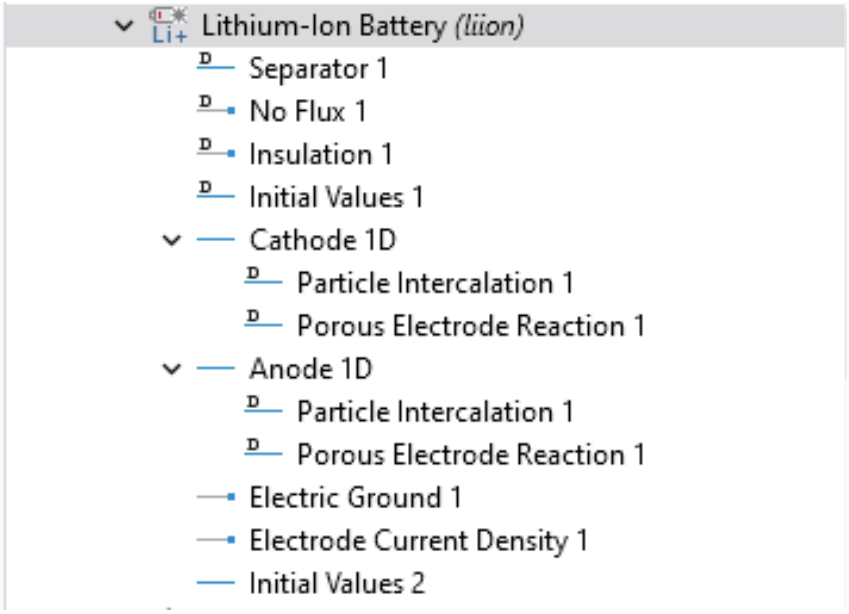

Fig. 4.7 Battery Design Module model tree

The three domains are assigned - with the corresponding material properties - to the proper geometry. For the two electrodes, the particle intercalation - based on Fick's law - and the porous reaction - based on Butler-Volmer equation - are properly set. The *No Flux* boundary condition refers to lithium ions flux and its imposed to electrode interface with their corresponding current collectors. The *Insulation* boundary condition refers to electrical insulation which is not present in the analyzed domain.

$$\frac{\partial c_l}{\partial z}\Big|_{z=0,z=L} = 0 \tag{4.5}$$

The electric ground is set to the anode current collector and the current density is applied to the cathode one as the ratio between the charging/discharging current and the crossed surface represented by the surface of the all layers. The crossed surface considers all the 144 layers and each layer has a 150x70mm^2 surface.

$$\Phi_s\Big|_{z=L} = 0 \tag{4.6}$$

$$i(z,t)\Big|_{z=0} = \frac{I}{A} \tag{4.7}$$

The two initial values correspond to the initial electric potentials (solid and liquid) and electrolyte salt concentration. Due to the electric ground, the solid electric potential is set to zero in the anode and separator while in the cathode is set to the difference between the cathode equilibrium potential and the anode one evaluated at their initial state of lithiation. The electrolyte potential is set to the anode initial OCP while the initial electrolyte salt concentration is set to 1000 mol/m^3.

4.2.3 Concentration in the solid phase

Once all the parameters and boundary conditions are set, the electrochemical analysis can be computed. The electrodes domain has been divided into intervals to extract the average lithium ions concentration - in time - within the electrode thickness as schematized in Figure 4.8. The reported example is with the cathode but the same is done with the anode with less points due to its length.

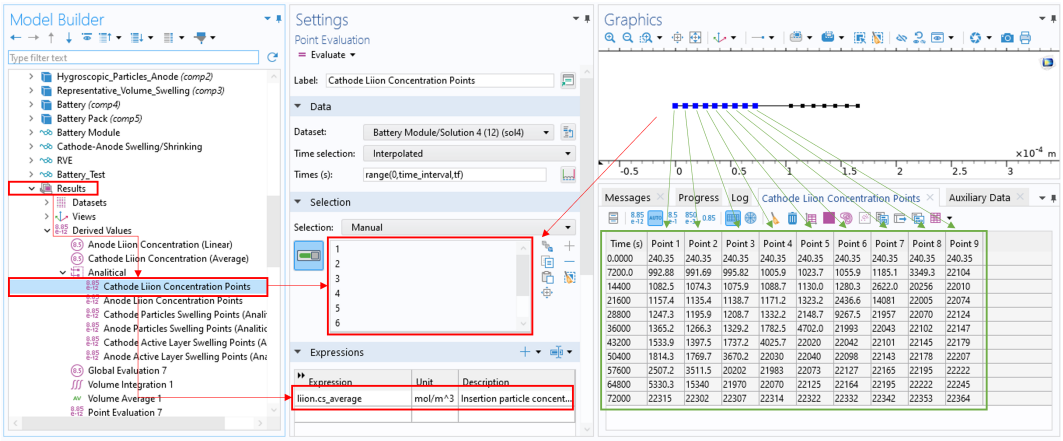

Fig. 4.8 Extraction of lithium ions concentration within the electrode domain - Cathode

4.3 Multiscale model

Once computed the lithium ions concentration in the solid phase within the electrode according to the current delivered by the battery for a certain amount of time, the chemically induced deformations to the active material particles and the consequently strains in the upper scales can be evaluated. A multi-scale model has been developed to analyze this strain evolution and account for the mechanical behaviour induced by the electrochemical process in structural simulation of the battery module.

As mentioned in the previous section, the particles swelling/shrinking can be easily computed in an analytical form as function of the concentration in the solid phase with the Equation 3.30. Even the electrode strain can be computed thanks to the porosity and the particle strains. This is true if there is no external pressure that significantly affects the porosity. In reality, a numerical way to evaluate the particle and electrode strain is evaluated: the representative volume elements of the active materials are composed by eight particles with the proper porosity; the particles are subjected to an *Hygroscopic Swelling* which models the chemical volumetric strain as shown in Figure 4.9. The implemented model is the Equation 3.30 but with two coefficients rather then one. It is sufficient to impose $\beta_h = 1$ and use the coherent unit of measure.

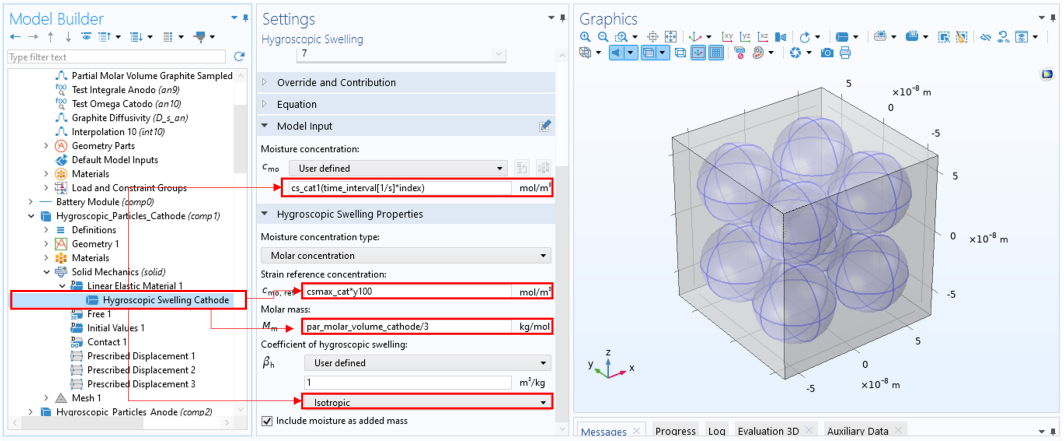

Fig. 4.9 Modeling of particles and electrodes strain

The swelling/shrinking is discretized in time iterating *index* which is multiplied by the time step. The reference concentration is fixed to the corresponding initial state of lithiation of the electrode because it correspond to $c_{s,0}$. The deformation of the RVE is extracted to compute the strain that should be imposed in the next scale. However, in this case, the analytical computation of the active layers strain allows a lower computational cost.

The electrodes strains are then coupled in a battery representative volume element composed by the two current collectors, the separator and the two active layers. Due to the small thickness of the electrodes with respect to their in-plane dimensions, a plane strain condition can be assumed:

$$\varepsilon^e_{in-plain} = \varepsilon^e_x = \varepsilon^e_y = 0 \quad ; \quad \varepsilon^e_{out-of-plane} = \varepsilon^e_z = \varepsilon^e_v \tag{4.8}$$

Therefore, an equivalent thermal strain has been applied to the electrodes domain to evaluate the overall battery strain. An example of equivalent thermal strain applied to the cathode is shown in Figure 4.10. The strain is applied just on z direction.

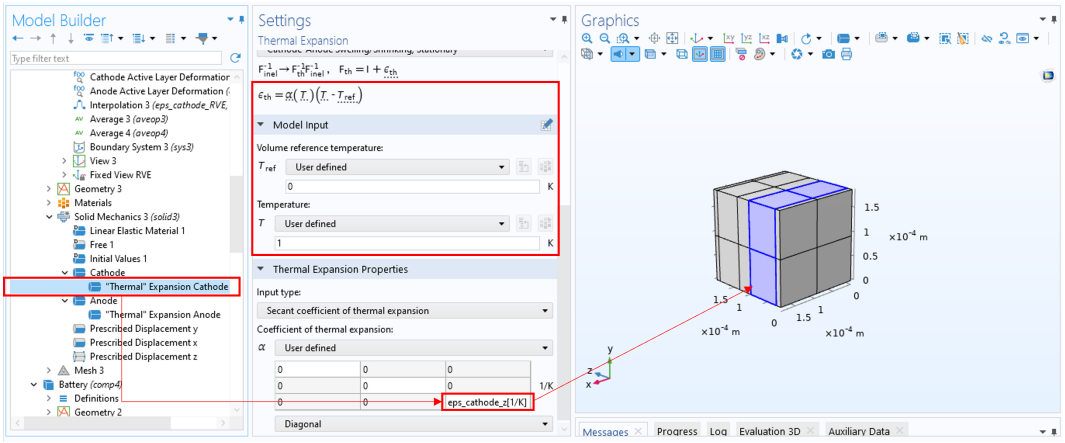

Fig. 4.10 Example of equivalent thermal strain applied to the electrode

To avoid rigid motion along x and y directions, the out-of-plane displacement of the middle planes parallel to yz and xz respectively has been imposed null due to symmetry. To avoid rigid motion along z direction, one of the two edges of the representative elementary cell has the z-displacement constrained. The mentioned boundary conditions are reported in Figure 4.11. Doing that, the battery strain can be evaluated as the ratio between the z-displacement of the other edge and the initial thickness of the elementary cell which is the sum of the thicknesses of its constituents (Equations 4.9 and 4.10).

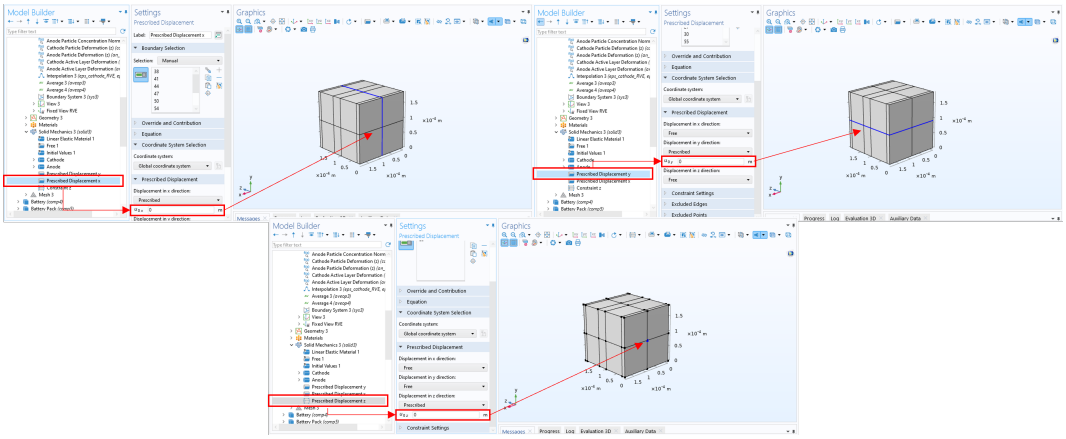

Fig. 4.11 RVE Boundary Conditions

$$\varepsilon_z^{batt} = \frac{\Delta t_{RVE}}{t_{0,RVE}} \tag{4.9}$$

$$t_{0,RVE} = t_{cc}^{cat} + t_{al}^{cat} + t_{sep} + t_{al}^{an} + t_{cc}^{an} \tag{4.10}$$

The computed battery strain is the input of the upper scales simulations. In particular, two analysis have been performed in the model. The first is at the single battery level to compare the numerical results with the experimental ones [51] to validate the electrochemical model. The second is at the battery module level to perform the structural analysis once homogenized. A workflow from the RVE strain coupling to the application of battery strain is shown in Figure 4.12. The COMSOL *non-local couplings* are used to achive multi-component and consequently multi-scale analysis. In this case, the *average* operation has been used in the free surface of the representative volume element to evaluate its displacement (w_3 in the figure) and consequently its strain. To apply this deformation in the upper scale, it is necessary to introduce the coupling *variable* in the next component.

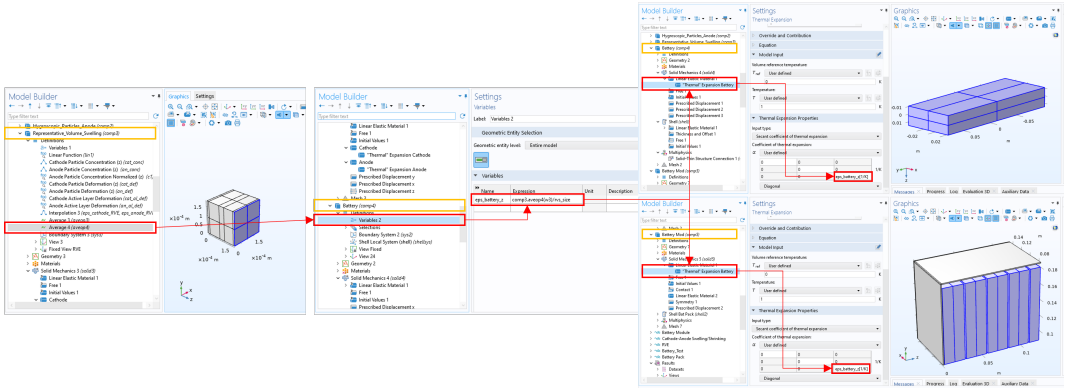

Fig. 4.12 Strain workflow with COMSOL non-local couplings

At the battery level, due to symmetry conditions, just an eighth of the battery can be simulated or - as already did with the elementary cell - the out-of-plane displacement of the symmetry planes can be constrained as shown in Figure 4.13 for the *xy* plane. Each battery is coverd by a thin aluminum case.

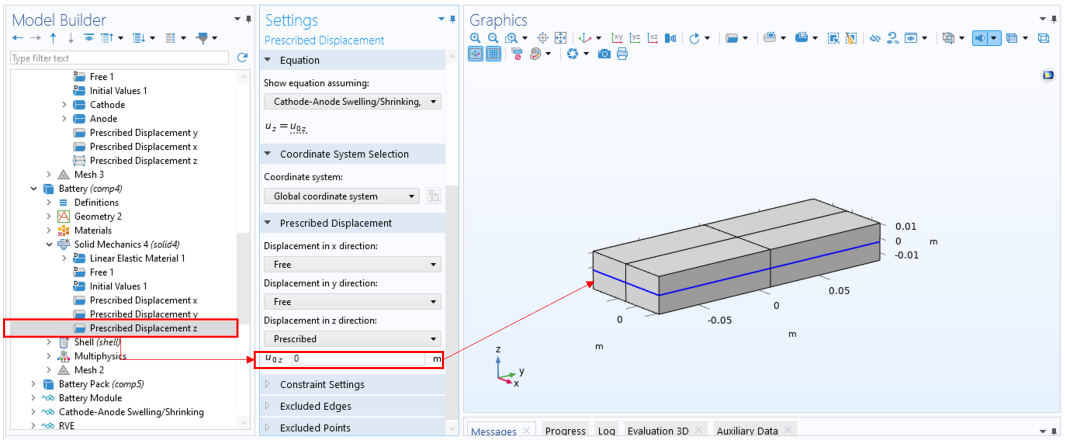

Fig. 4.13 Example of battery symmetry boundary condition

The thickness change is finally evaluated - due to symmetry - as two times the displacement of the surface middle point.

The battery module geometry consists in a regular sequence of batteries inside a case of the whole module. The geometrical parameters - apart from the single battery ones - are the space between the batteries, the space between the batteries and the case, the case material and thickness. The mechanical parameters of the aluminum case and of the module case are reported in Table 4.3. The dimensions of the battery module case are not reported because they depend on the variable gap. Also in this case study, focusing just on the mechanical behaviour due to the electrochemical operating conditions, an eighth of the system can be considered due to symmetry as reported in Figure 4.14.

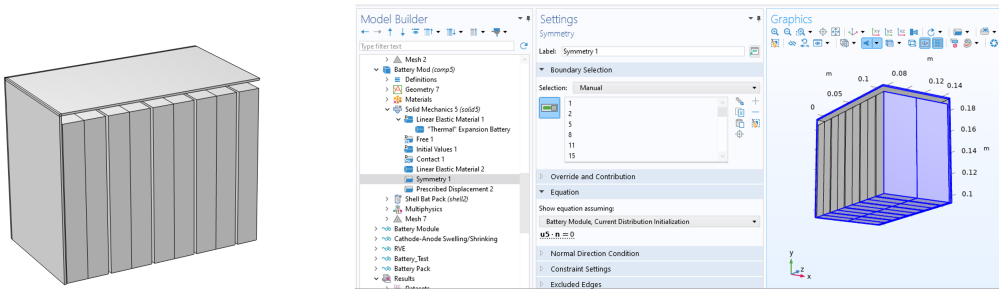

(a) (b)

Fig. 4.14 Battery pack domain

Table 4.3 Battery case and module case parameters

Domain	Property	Symbol	Value	Unit
Battery Case	Young's Modulus	E_{case}^{bat}	70	GPa
	Poisson's ratio	ν_{case}^{bat}	0.3	-
	Thickness	t_{case}^{bat}	0.8	mm
	Width	w_{case}^{bat}	70	mm
	Height	h_{case}^{bat}	27	mm
	Length	l_{case}^{bat}	185	mm
Module Case	Young's Modulus	E_{case}^{mod}	210	GPa
	Poisson's ratio	ν_{case}^{mod}	0.3	-
	Thickness	t_{case}^{mod}	1.2	mm

In the module there is no more symmetry in the single battery middle plane because each battery displacement is influenced by the other. Therefore the contact between the batteries is modelled with the penalty function: it is a method used in computational simulations, to model interactions between two bodies that come into contact. Penalty-based contact modeling imposes a "penalty" (or artificial stiffness) when two surfaces come into contact or overlap. It creates a resistance force that increases proportionally with the amount of penetration between the contacting bodies.

Due to the prismatic regular shape of the batteries and their RVE, an hexahedral mesh is used. To minimize the error, the size of the hexahedra is chosen regularizing the ratio between their sides (Figure 4.15). The linear hexahedron is a 8-node element whose shape function are linear as shown in Figure 4.16. Second order elements are used in the model to avoid extra fine mesh. Additionally, with these regular shapes, the serendipity second order hexahedron performs very well and it is a 20-node element with respect to the second order Lagrange hexahedron which is a 27-node element. Instead, each battery aluminum case can be meshed with shell elements due to their small thickness. Even the module case can be meshed with shell elements but the model aims to use also the case stiffness as design parameter: tougher plates can be simulated.

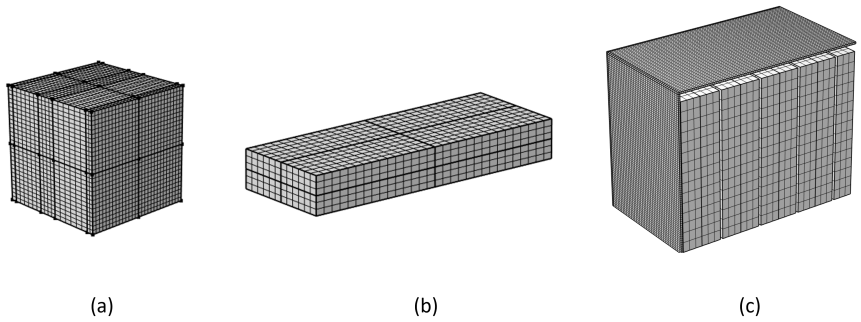

Fig. 4.15 Hexahedral mesh

NODE POINT P	SHAPE FUNCTION
(0,0,0)	$(1-\xi_1)(1-\xi_2)(1-\xi_3)$
(1,0,0)	$\xi_1(1-\xi_2)(1-\xi_3)$
(0,1,0)	$(1-\xi_1)\xi_2(1-\xi_3)$
(1,1,0)	$\xi_1\xi_2(1-\xi_3)$
(0,0,1)	$(1-\xi_1)(1-\xi_2)\xi_3$
(1,0,1)	$\xi_1(1-\xi_2)\xi_3$
(0,1,1)	$(1-\xi_1)\xi_2\xi_3$
(1,1,1)	$\xi_1\xi_2\xi_3$

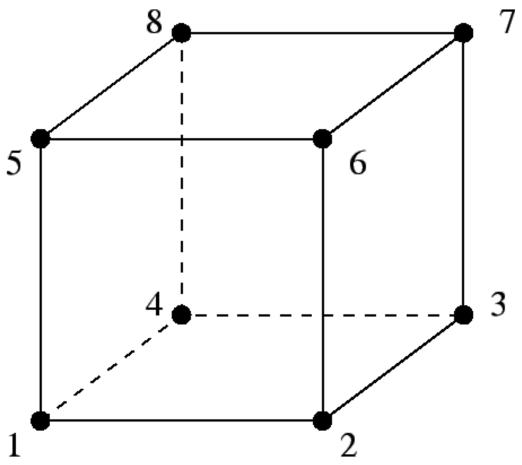

Fig. 4.16 Linear hexahedron shape functions

Thanks to the *Solid-Thin Structure Coupling*, the two elements' displacement fields are connected. There are several options of connection but due to the geometry and meshing choice, the *Shared Boundaries* feature is used (Figure 4.17): the shell are constructed as the internal battery cover as it really is.

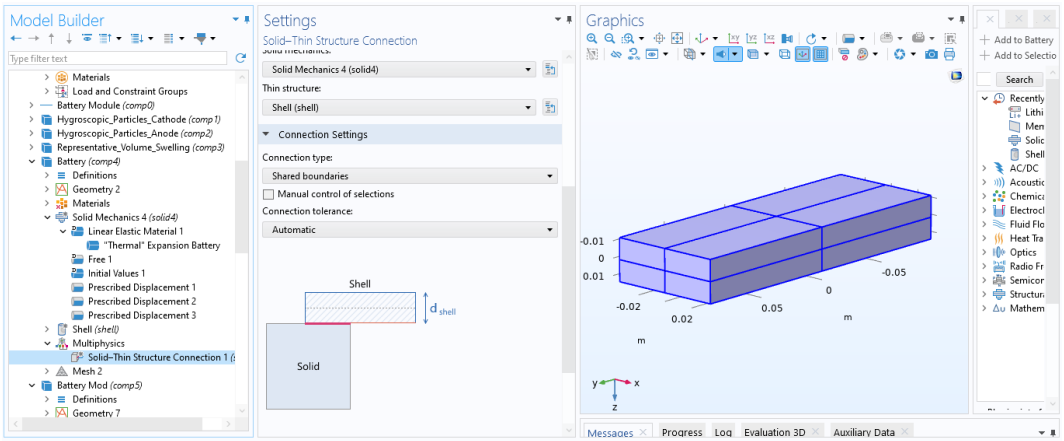

Fig. 4.17 Solid-Shell coupling

Figure 4.18 summarize the implemented from the lithium ions concentration across the electrode thickness to the macro-scale deformation.

Microscale	Mesoscale	Macroscale
Input Mean solid phase concentration inside the active material particle $c_{s,avg}$	**Input** Active material RVE volumetric strain ε_v^e	**Input** Battery RVE strain ε_v^{batt}
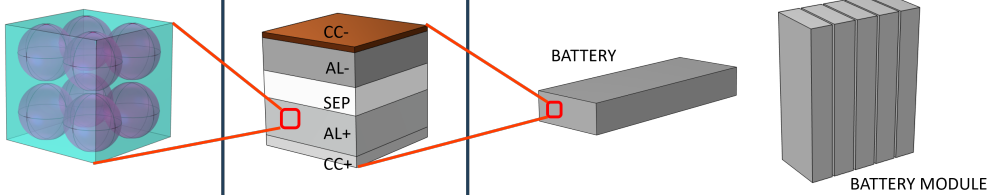		
Output Particle and electrode volumetric strain $\varepsilon_v^p, \varepsilon_v^e$	**Output** Battery RVE strain ε_v^{batt}	**Output** Deformation of the single battery and evaluation of the stress and strain of the entire battery module

Fig. 4.18 Multi-scale model workflow

Chapter 5

Results

In this chapter, the multiscale model is validated comparing the corresponding numerical results with the experimental measurement conducted on LFP batteries. The comparison involves the battery voltage and thickness change measured and computed at different C-rates of charging and discharging.

Additionally, the designed model is applied to a battery module consisting of two rows of 9 LFP batteries each. After the homogenization of the battery's mechanical properties, a structural analysis is performed to evaluate the gap between the batteries - considered as design parameter - in the worst case scenario of reversible swelling.

5.1 Experiment

Three samples of prismatic LFP/graphite lithium-ion batteries have been tested - using a dedicated setup - to assess their performance. The batteries are subjected to various charge and discharge currents while voltage, temperature and deformation are measured. Charge rates range span from C/20 to C/2, while discharge rates range from C/20 to 3C, following manufacturer specifications avoiding high charge C-rates. Each test is performed five times and consist in a full charge/discharge in the SOC range 0%-100%. The thickness variation of the battery is measured with laser sensors and all the tests are performed in a thermostatic chamber to set a constant temperature at 20°C. A scheme of the test setup is shown in Figure 5.1 [51].

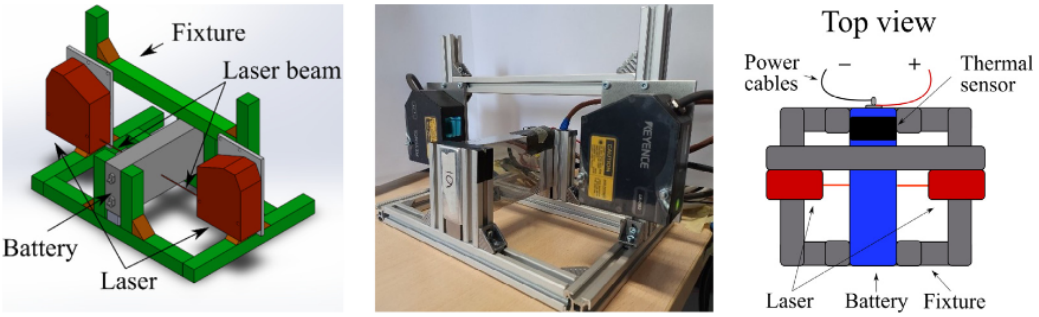

Fig. 5.1 Experimental measurement setup [51]

Additionally, images of the internal structure of the electrodes have been taken with a scanning electron microscope (SEM). These are reported in Figure 5.2 [6] and the geometrical properties are crucial for the design of the RVE and consequently the homogenization and the multi-scale evaluation of the deformation.

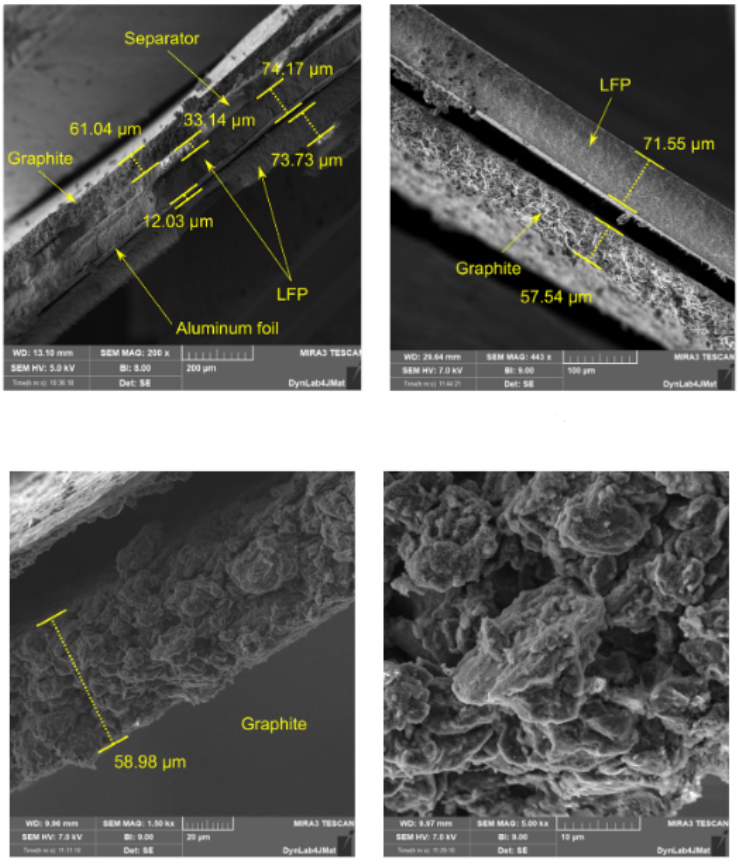

Fig. 5.2 Internal structure of electrodes from SEM images [6]

5.2 Multiscale model validation

The measured voltage and the computed one from the multi-scale model are compared at different C-rates as shown in Figure 5.3.

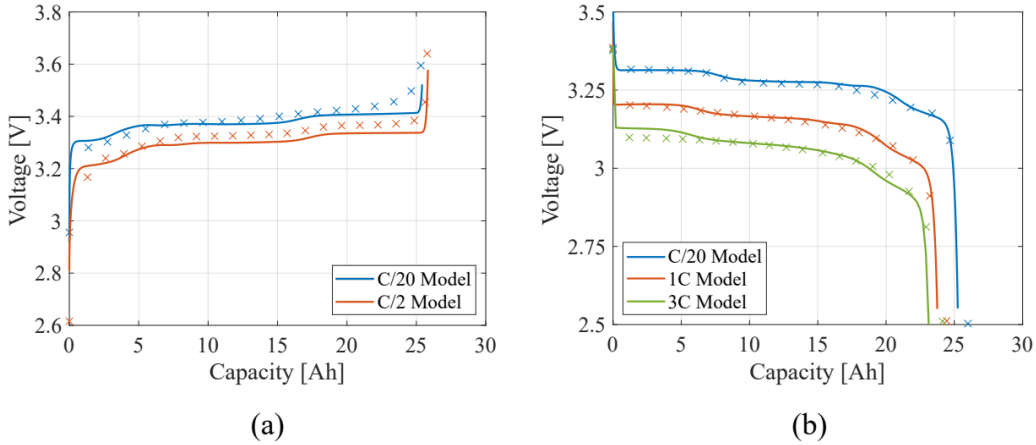

Fig. 5.3 Voltage comparison between model results (solid line) and experimental measurements (crosses) in (a) charge and (b) discharge

The comparison shows a good agreement confirming the validity of the electrochemical model whose output is the lithium ion concentration within the electrode thickness which is the origin of the microscopic deformation and therefore, the input of the multi-scale mechanical model. The behaviour of the mentioned concentration in the solid phase is shown in Figure 5.4 during a C/20 charge/discharge rate as example.

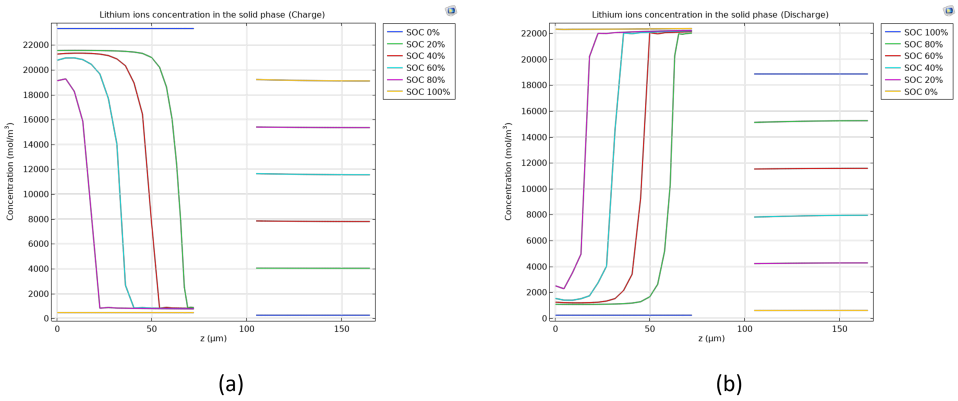

Fig. 5.4 Lithium ion concentration in the electrodes during (a) charge and (b) discharge

According to what has been said in Paragraph 3.2.1, the lithiated-electrode has higher concentration in the areas closer to the separator and vice versa for the delithiated one. Once the concentration from the electrode thickness is extracted, the two active layers are subjected to their corresponding deformations that are then coupled in the elementary cell representative volume element as reported in Figures 5.5 and 5.6.

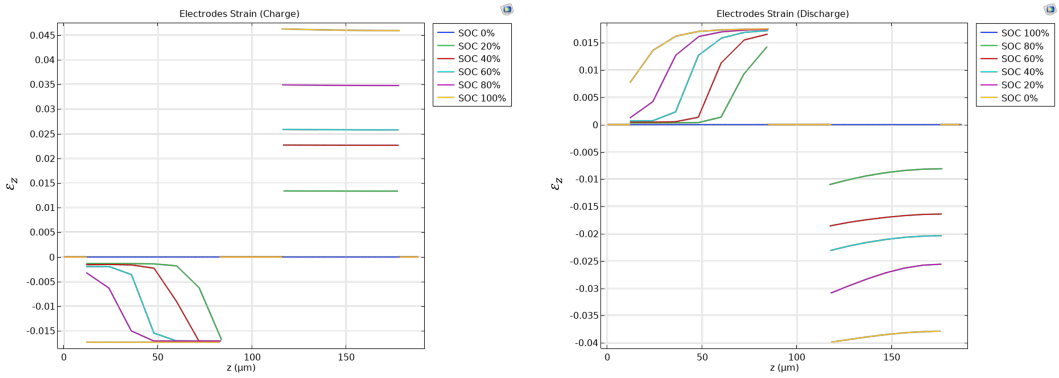

(a) (b)

Fig. 5.5 Electrodes strain coupling during (a) charge and (b) discharge

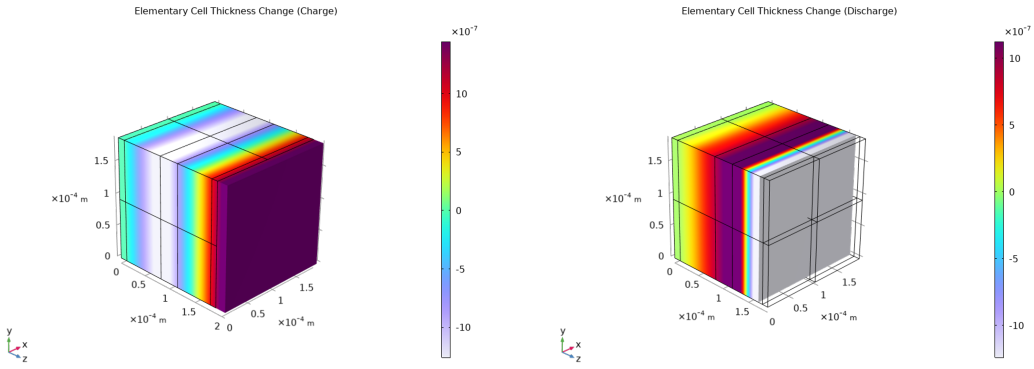

(a) (b)

Fig. 5.6 Example of RVE deformation during (a) charge and (b) discharge

At this point - evaluated the battery strain with the Equation 4.9 - the battery thickness change in time can be computed and compared to the experimental one thanks to the implemented *non-local coupling*. The results are plotted in Figure 5.7.

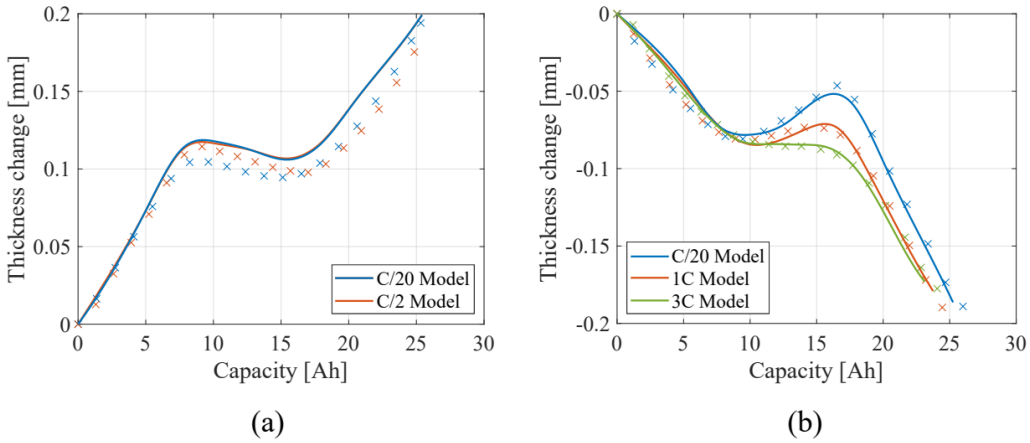

Fig. 5.7 Thickness change comparison between model results (solid line) and experimental measurements (crosses) in (a) charge and (b) discharge

The model is satisfactory as the comparison shows a good match of the numerical results with the experimental measurements of the macroscopic deformation. Implementing the graphite partial molar volume as function of the lithiation index and the current rates - as described in Paragraph 3.3.1 - the dependency of the thickness change on the C-rates in discharge is catched by the model (Figure 5.7b). The responsible of this behaviour is the transition to stage IIL of graphite that appears at low discharge rates affecting the structural deformation of the graphite crystalline structure. In Figure 5.8 is presented the maximum reversible displacement reached at the end of the charge and discharge. An half of the battery is figured to appreciate the solution variable also in the bottom part of the battery.

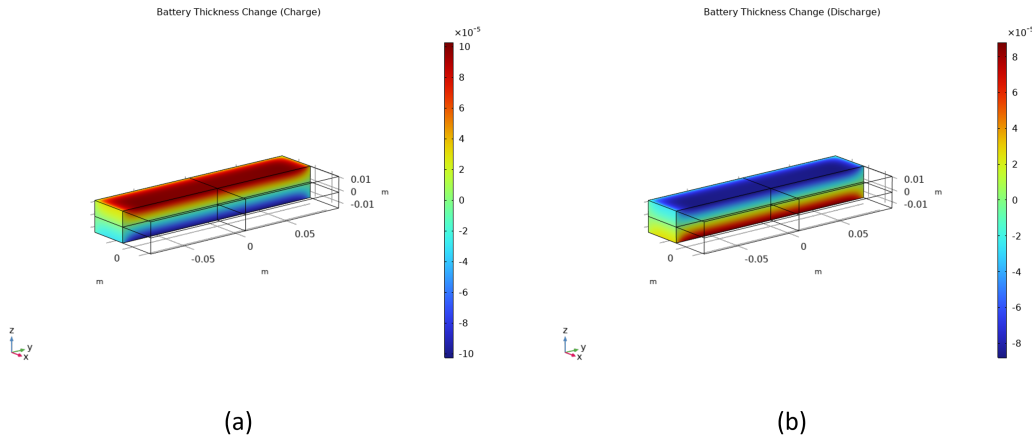

Fig. 5.8 Thickness change at the end of the (a) charge and (b) discharge

5.3 Battery module

The structural behaviour of a 60V battery module - consisting by 18 LFP/graphite batteries - is studied to investigate how the strain of each battery affects the deformation and the stress in the module. The case of the battery module is made of structural steel plates, 1.2 mm thick. Two design solutions of the battery module are studied varying the battery arrangements:

1. Batteries are packed with no gap between them.
2. A 0.5 mm gap is left between the batteries. Such gap could be smaller, at the limit equal to an half of the reversible deformation computed or measured of each single battery (almost 0.2 mm in this case study). Nevertheless, from a constructive point of view, it would be difficult to leave such a small gap. For this reason, 0.5 mm is chosen as a realistic and conservative scenario.

In the first design solution, the reversible deformation of the batteries during charge and discharge causes severe deformation in the case of the battery module - as reported in Figure 5.9a - and higher stress within each battery cell as reported in Figure 5.10a and 5.11a. In the second design solution, the gap between the batteries entirely accomodates the reversible swelling obtained during charge, mitigating the stress within the cell and avoiding the deformation of the external casing of the battery module.

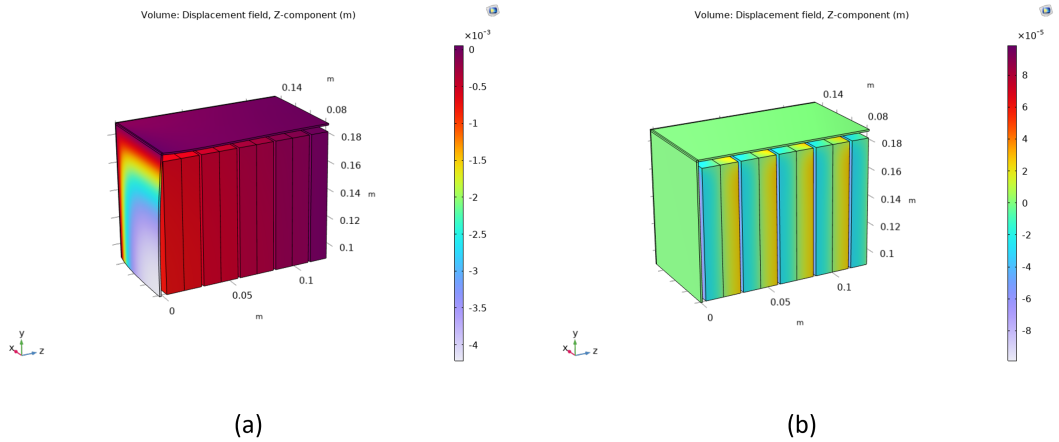

(a) (b)

Fig. 5.9 Displacement of the battery module in (a) solution 1 and (b) solution 2

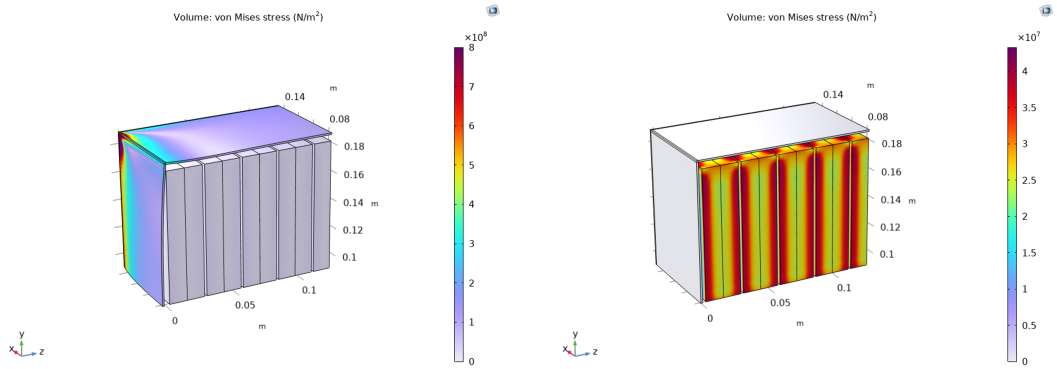

Fig. 5.10 Von Mises stress of the battery module in (a) solution 1 and (b) solution 2

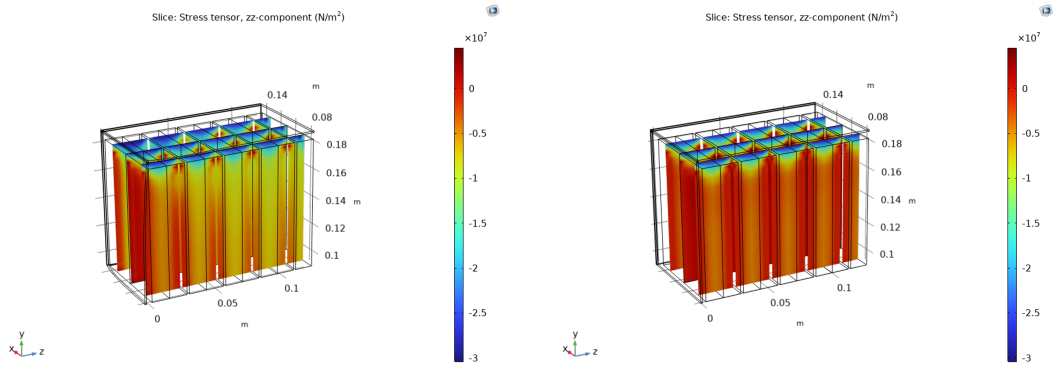

Fig. 5.11 Stress in batteries' thickness direction in (a) solution 1 and (b) solution 2

Figure 5.11 shows the stress in the z direction in three cross-sections - parallel to the *xz* plane - inside the batteries. Design solution 1 (Figure 5.11a) results in a more severe compressive stress within the batteries because of the constrained expansion with respect to the design solution 2 (Figure 5.11b). Nevertheless, the top and the bottom of the case of the batteries acts as a membrane stiffness and constrains the expansion in the z direction of the battery internal, giving rise to high and localized compressive stress. Just an eighth of the battery module is explicitly simulated thanks to symmetry, so the bottom of the battery module is not shown in the results. On the other hand, the case acts as a flexural stiffness on the large surfaces of the batteries, giving a lower constraint, allowing the deformation of the battery internal and consequently lowering the stress.

The price to be paid for the design solution 2 is the increased size of the battery module and the consequent decrease in its energy and power density. In fact, the volume of the module pass from 6.9 dm^3 in design solution 1 to 7.3 dm^3 in the design solution 2 with an increase of only 6% in volume, and therefore an equal percentage reduction in energy and power density. From these considerations, it turns out that it is beneficial to consider the reversible deformation of the batteries during operation in the design of the battery module, as a modest increase in the battery module volume allows to mitigate the structural issues given by the battery deformation, causing stress in the battery itself and in the casing of the module.
Such gap is not beneficial only from the structural point of view, but it gives benefits also to thermal management of the battery module, as it provides greater space for cooling.

Chapter 6

Conclusions

After a deep investigation on the numerical approach for solving PDEs, on the homogenization theory and the multiphysics coupling on the Doyle-Fuller-Newman model, an homogenization-based multiscale model is developed in COMSOL Multiphysics to involve batteries and battery modules in structural analysis during their operating conditions.

Through the lithium ions concentration within the electrode thickness, the induced chemical deformation is followed from particle scale to the battery one thanks to the developed multiscale model which is validated through experimental measurements conducted on LFP/graphite prismatic LIB samples. The voltage and thickness change are compared at different C-rates demonstrating a good fit of the model results to the experimental measurements.

The mechanical consequences in terms of stress field can be evaluated through a the two-step homogenization: the nano-structured active materials are homogenized inside the layered battery representative volume element which is likewise homogenized to compute the battery's mechanical properties.

Combining the multiscale model and the homogenization-based approach allows for a comprehensive study of the battery module, accounting for both the internal electrochemical processes and the external boundary conditions. This integrated analysis is crucial for the optimization of battery packs, enabling more efficient design, enhanced performance, and improved safety under various operating conditions.

In this work, the model is applied to a 60V LFP/graphite battery module investigating the influence of the gap between batteries during their operating conditions. A small gap of 0.5 mm results is best compromise: it is sufficient to entirely accomodate the reversible swelling, reduce internal battery stress and introduce space for cooling; the price to be paid is a modest 6% increase in volume and consequently the same decrease in energy and power density.

Bibliography

[1] Arun Patil et al. “Issue and challenges facing rechargeable thin film lithium batteries”. en. In: *Materials Research Bulletin* 43.8-9 (Aug. 2008), pp. 1913–1942. ISSN: 00255408. DOI: 10.1016/j.materresbull.2007.08.031. URL: https://linkinghub.elsevier.com/retrieve/pii/S0025540807003868 (visited on 09/20/2024).

[2] JIlin Chen, Xuanyao Huang, and Honglin Wang. “Lithium Battery, About Its History, Future Development, Environmental Impact and System Economics:” en. In: Kunming, China, 2022. DOI: 10.2991/assehr.k.220110.021. URL: https://www.atlantis-press.com/article/125969424 (visited on 09/20/2024).

[3] Salvatore Martelli, Francesco Mocera, and Aurelio Somà. “Carbon footprint of an orchard tractor through a life-cycle assessment approach”. In: *Agriculture* 13.6 (2023), p. 1210.

[4] Salvatore Martelli et al. “Life Cycle Assessment Comparison of Orchard Tractors Powered by Diesel and Hydrogen Fuel Cell”. In: *Energies* 17.18 (2024), p. 4599.

[5] Hanna Vikström, Simon Davidsson, and Mikael Höök. “Lithium availability and future production outlooks”. en. In: *Applied Energy* 110 (Oct. 2013), pp. 252–266. ISSN: 03062619. DOI: 10.1016/j.apenergy.2013.04.005. URL: https://linkinghub.elsevier.com/retrieve/pii/S0306261913002997 (visited on 09/20/2024).

[6] Davide Clerici, Francesco Mocera, and Aurelio Soma. “Electrochemical–mechanical multi-scale model and validation with thickness change measurements in prismatic lithium-ion batteries”. In: *Journal of Power Sources* 542 (2022), p. 231735.

[7] Peyman Mohtat et al. “Differential Expansion and Voltage Model for Li-ion Batteries at Practical Charging Rates”. In: *Journal of The Electrochemical Society* 167.11 (2020), p. 110561. ISSN: 1945-7111. DOI: 10.1149/1945-7111/aba5d1.

[8] Daniel Sauerteig et al. “Electrochemical-mechanical coupled modeling and parameterization of swelling and ionic transport in lithium-ion batteries”. In: *Journal of Power Sources* 378 (2018), pp. 235–247.

[9] Davide Clerici and Francesco Mocera. “Experimental Characterization of Lithium-Ion Cell Strain Using Laser Sensors”. In: *Energies* (2021).

[10] Shankar Mohan et al. “A phenomenological model of bulk force in a li-ion battery pack and its application to state of charge estimation”. In: *Journal of the Electrochemical Society* 161.14 (2014), A2222.

[11] Miriam A Figueroa-Santos, Jason B Siegel, and Anna G Stefanopoulou. “Leveraging Cell Expansion Sensing in State of Charge Estimation: Practical Considerations”. In: *Energies* 13.10 (2020), p. 2653.

[12] Ajay Raghavan et al. “Embedded fiber-optic sensing for accurate internal monitoring of cell state in advanced battery management systems part 1: Cell embedding method and performance”. In: *Journal of Power Sources* 341 (2017), pp. 466–473.

[13] Anurag Ganguli et al. “Embedded fiber-optic sensing for accurate internal monitoring of cell state in advanced battery management systems part 2: Internal cell signals and utility for state estimation”. In: *Journal of Power Sources* 341 (2017), pp. 474–482. ISSN: 03787753. DOI: 10.1016/j.jpowsour.2016.11.103. URL: http://dx.doi.org/10.1016/j.jpowsour.2016.11.103.

[14] Micael Nascimento et al. “Internal strain and temperature discrimination with optical fiber hybrid sensors in Li-ion batteries”. In: *Journal of Power Sources* 410-411.October 2018 (2019), pp. 1–9. ISSN: 03787753. DOI: 10.1016/j.jpowsour.2018.10.096. URL: https://doi.org/10.1016/j.jpowsour.2018.10.096.

[15] Lisa K Willenberg et al. “High-precision monitoring of volume change of commercial lithium-ion batteries by using strain gauges”. In: *Sustainability* 12.2 (2020), p. 557.

[16] Jessica Hemmerling, Alexander Fill, and Kai Peter Birke. “Analysis of the age-, current-and temperature-dependent expansion of cylindrical NCM| Graphite Li-ion battery cells using strain gauges”. In: *Journal of Energy Storage* 99 (2024), p. 113177.

[17] Julius Schmitt et al. “Measurement of gas pressure inside large-format prismatic lithium-ion cells during operation and cycle aging”. In: *Journal of Power Sources* 478 (2020), p. 228661.

[18] Severin Hahn et al. “Pressure Prediction Modeling and Validation for Lithium-Ion Pouch Cells in Buffered Module Assemblies”. In: *Journal of Energy Storage* 40 (2021), p. 102517.

[19] Lukas Gold et al. “Probing lithium-ion batteries’ state-of-charge using ultrasonic transmission – Concept and laboratory testing”. In: *Journal of Power Sources* 343 (2017), pp. 536–544. ISSN: 03787753. DOI: 10.1016/j.jpowsour.2017.01.090. URL: http://dx.doi.org/10.1016/j.jpowsour.2017.01.090.

[20] Priyank Gupta and Peter Gudmundson. “A multi-scale model for simulation of electrochemically induced stresses on scales of active particles, electrode layers, and battery level in lithium-ion batteries”. In: *Journal of Power Sources* 511 (2021), p. 230465.

[21] Priyank Gupta and Peter Gudmundson. “Modeling of local electrode stresses and pressures in lithium-ion battery packs using three-dimensional homogenization”. In: *Journal of Power Sources* 582 (2023), p. 233514.

[22] Naoki Nitta et al. “Li-ion battery materials: present and future”. en. In: *Materials Today* 18.5 (June 2015), pp. 252–264. ISSN: 13697021. DOI: 10.1016/j.mattod.2014.10.040. URL: https://linkinghub.elsevier.com/retrieve/pii/S1369702114004118 (visited on 09/11/2024).

[23] Liang Wang et al. “Recent advances in interface engineering of silicon anodes for enhanced lithium-ion battery performance”. In: *Energy Storage Materials* 66 (2024), p. 103243. ISSN: 2405-8297. DOI: https://doi.org/10.1016/j.ensm.2024.103243. URL: https://www.sciencedirect.com/science/article/pii/S2405829724000709.

[24] Sana Kainat et al. “Electrolytes in Lithium-Ion Batteries: Advancements in the Era of Twenties (2020’s)”. In: *Materials Chemistry and Physics* 313 (2024), p. 128796. ISSN: 0254-0584. DOI: https://doi.org/10.1016/j.matchemphys.2023.128796. URL: https://www.sciencedirect.com/science/article/pii/S0254058423015043.

[25] Niranjanmurthi Lingappan et al. “A comprehensive review of separator membranes in lithium-ion batteries”. In: *Renewable and Sustainable Energy Reviews* 187 (2023), p. 113726. ISSN: 1364-0321. DOI: https://doi.org/10.1016/j.rser.2023.113726. URL: https://www.sciencedirect.com/science/article/pii/S136403212300583X.

[26] Qian Wang et al. “A critical review of thermal management models and solutions of lithium-ion batteries for the development of pure electric vehicles”. In: *Renewable and Sustainable Energy Reviews* 64 (2016), pp. 106–128. ISSN: 1364-0321. DOI: https://doi.org/10.1016/j.rser.2016.05.033. URL: https://www.sciencedirect.com/science/article/pii/S1364032116301435.

[27] Xuning Feng et al. “Thermal runaway mechanism of lithium ion battery for electric vehicles: A review”. In: *Energy Storage Materials* 10 (2018), pp. 246–267. ISSN: 2405-8297. DOI: https://doi.org/10.1016/j.ensm.2017.05.013. URL: https://www.sciencedirect.com/science/article/pii/S2405829716303464.

[28] A. Gugliotta, A. Somà, and N. Zampieri. *Elementi finiti*. Quine, 2022. ISBN: 9788831284066. URL: https://books.google.it/books?id=NoNFzwEACAAJ.

[29] D.T. Wadiak. “Application of the finite-element method to the diffusion and reaction of chemical species in multilayered polymeric bodies”. en. In: *Mathematical Modelling* 7.2-3 (1986), pp. 385–395. ISSN: 02700255. DOI: 10.1016/0270-0255(86)90059-X. URL: https://linkinghub.elsevier.com/retrieve/pii/027002558690059X (visited on 09/13/2024).

[30] W. Voigt. “Ueber die Beziehung zwischen den beiden Elasticitätsconstanten isotroper Körper”. In: *Annalen der Physik* 274.12 (Jan. 1889), pp. 573–587. DOI: 10.1002/andp.18892741206.

[31] Andreas Reuß. “Berechnung der Fließgrenze von Mischkristallen auf Grund der Plastizitätsbedingung für Einkristalle .” In: *Zamm-zeitschrift Fur Angewandte Mathematik Und Mechanik* 9 (), pp. 49–58. URL: https://api.semanticscholar.org/CorpusID:122637382.

[32] John C. Halpin. “Effects of Environmental Factors on Composite Materials.” In: 1969. URL: https://api.semanticscholar.org/CorpusID:135872649.

[33] Manh-Kien Tran et al. "A comprehensive equivalent circuit model for lithium-ion batteries, incorporating the effects of state of health, state of charge, and temperature on model parameters". In: *Journal of Energy Storage* 43 (2021), p. 103252. ISSN: 2352-152X. DOI: https://doi.org/10.1016/j.est.2021.103252. URL: https://www.sciencedirect.com/science/article/pii/S2352152X2100949X.

[34] Marc Doyle, Thomas F Fuller, and John Newman. "Modeling of galvanostatic charge and discharge of the lithium/polymer/insertion cell". In: *Journal of the Electrochemical society* 140.6 (1993), p. 1526.

[35] Thomas F Fuller, Marc Doyle, and John Newman. "Simulation and optimization of the dual lithium ion insertion cell". In: *Journal of the Electrochemical Society* 141.1 (1994), p. 1.

[36] Wei Sun et al. "Determination of the tortuosity of a Li-ion battery separator". en. In: *Journal of Energy Storage* 97 (Sept. 2024), p. 112940. ISSN: 2352152X. DOI: 10.1016/j.est.2024.112940. URL: https://linkinghub.elsevier.com/retrieve/pii/S2352152X2402526X (visited on 09/02/2024).

[37] Raimund Koerver et al. "Chemo-mechanical expansion of lithium electrode materials–on the route to mechanically optimized all-solid-state batteries". In: *Energy & Environmental Science* 11.8 (2018), pp. 2142–2158.

[38] Christophe Didier et al. "Phase Evolution and Intermittent Disorder in Electrochemically Lithiated Graphite Determined Using in Operando Neutron Diffraction". In: *Chemistry of Materials* 32.6 (2020), pp. 2518–2531. ISSN: 15205002. DOI: 10.1021/acs.chemmater.9b05145.

[39] Sou Taminato et al. "Real-time observations of lithium battery reactions—operando neutron diffraction analysis during practical operation". In: *Scientific reports* 6.1 (2016), pp. 1–12.

[40] Davide Clerici, Francesco Mocera, and Aurelio Somà. "Analytical solution for coupled diffusion induced stress model for lithium-ion battery". In: *Energies* 13.7 (2020). ISSN: 19961073. DOI: 10.3390/en13071717.

[41] Parthasarathy M Gomadam and John W Weidner. "Modeling volume changes in porous electrodes". In: *Journal of The Electrochemical Society* 153.1 (2005), A179.

[42] Bin Wu and Wei Lu. "A consistently coupled multiscale mechanical–electrochemical battery model with particle interaction and its validation". en. In: *Journal of the Mechanics and Physics of Solids* 125 (Apr. 2019), pp. 89–111. ISSN: 00225096. DOI: 10.1016/j.jmps.2018.12.005. URL: https://linkinghub.elsevier.com/retrieve/pii/S0022509618309141 (visited on 08/28/2024).

[43] Yue Qi et al. "Lithium Concentration Dependent Elastic Properties of Battery Electrode Materials from First Principles Calculations". In: *Journal of The Electrochemical Society* 161.11 (Aug. 2014), F3010. DOI: 10.1149/2.0031411jes. URL: https://dx.doi.org/10.1149/2.0031411jes.

[44] Jake Christensen and John Newman. "Stress Generation and Fracture in Lithium Insertion Materials". In: *Journal of Solid State Electrochemistry* 10 (May 2006), pp. 293–319. DOI: 10.1007/s10008-006-0095-1.

[45] Elham Sahraei et al. “Microscale failure mechanisms leading to internal short circuit in Li-ion batteries under complex loading scenarios”. In: *Journal of Power Sources* 319 (2016), pp. 56–65. ISSN: 0378-7753. DOI: https://doi.org/10.1016/j.jpowsour.2016.04.005. URL: https://www.sciencedirect.com/science/article/pii/S0378775316303469.

[46] Arpit Maheshwari et al. “Inverse parameter determination in the development of an optimized lithium iron phosphate – Graphite battery discharge model”. en. In: *Journal of Power Sources* 307 (Mar. 2016), pp. 160–172. ISSN: 03787753. DOI: 10.1016/j.jpowsour.2015.12.111. URL: https://linkinghub.elsevier.com/retrieve/pii/S0378775315307230 (visited on 08/26/2024).

[47] Jake Christensen and John Newman. “Stress Generation and Fracture in Lithium Insertion Materials”. In: *Journal of Solid State Electrochemistry* 10 (May 2006), pp. 293–319. DOI: 10.1007/s10008-006-0095-1.

[48] C Delacourt and M Safari. “Analysis of lithium deinsertion/insertion in LiyFePO4 with a simple mathematical model”. In: *Electrochimica Acta* 56.14 (2011), pp. 5222–5229.

[49] Paul W. C. Northrop et al. “Coordinate Transformation, Orthogonal Collocation, Model Reformulation and Simulation of Electrochemical-Thermal Behavior of Lithium-Ion Battery Stacks”. In: *Journal of The Electrochemical Society* 158.12 (Nov. 2011), A1461. DOI: 10.1149/2.058112jes. URL: https://dx.doi.org/10.1149/2.058112jes.

[50] Chunsheng Wang, Uday Kasavajjula, and Pedro Arce. “A Discharge Model for Phase Transformation Electrodes: Formulation, Experimental Validation, and Analysis”. In: *Journal of Physical Chemistry C* 111 (Nov. 2007). DOI: 10.1021/jp074490u.

[51] Davide Clerici et al. “Mechanical characterization of lithium-ion batteries with different chemistries and formats”. In: *Journal of Energy Storage* 84 (2024), p. 110899.